D-β-hydroxybutyrate stabilizes hippocampal CA3-CA1 circuit during acute insulin resistance.

Bartosz Kula[1], Botond Antal[2,3], Corey Weistuch[4], Florian Gackière[5], Alexander Barre[5], Victor Velado[6], Jeffrey M Hubbard[5], Maria Kukley[7,8], Lilianne R Mujica-Parodi[2,3,9,*], and Nathan A Smith[1,6,10,*].

1 Del Monte Institute for Neuroscience, Department of Neuroscience, University of Rochester, School of Medicine and Dentistry, Rochester, USA

2 Department of Biomedical Engineering, Stony Brook University, Stony Brook, USA

3 Athinoula A. Martinos Center for Biomedical Imaging, Massachusetts General Hospital and Harvard Medical School, Boston, USA

4 Department of Medical Physics, Memorial Sloan Kettering Cancer Center, New York, NY, USA

5 Neuroservices Alliance, Les Jardins de l'Entreprise, Quartier de le Confrérie, Le Puy Ste Réparade, France

6 Center for Neuroscience Research, Children's National Research Institute, Children's National Hospital, Washington D.C., USA

7 Achucarro Basque Center for Neuroscience, Leioa, Spain

8 Ikerbasque - Basque Foundation for Science, Bilbao, Spain

9 Laufer Center for Physical and Quantitative Biology, Stony Brook University, Stony Brook, USA

10 George Washington University School of Medicine and Health Sciences, Washington D.C., USA

* Corresponding authors: lilianne.strey@stonybrook.edu (LMP);
Nathan_Smith@urmc.rochester.edu (NAS)

1. **Abstract**

The brain primarily relies on glycolysis for mitochondrial respiration but switches to alternative fuels such as ketone bodies (KBs) when less glucose is available. Neuronal KB uptake, which does not rely on glucose transporter 4 (GLUT4) or insulin, has shown promising clinical applicability in alleviating the neurological and cognitive effects of disorders with hypometabolic components. However, the specific mechanisms by which such interventions affect neuronal functions are poorly understood. In this study, we pharmacologically blocked GLUT4 to investigate the effects of exogenous KB D-β-hydroxybutyrate (D-βHb) on mouse brain metabolism during acute insulin resistance (AIR). We found that both AIR and D-βHb had distinct impacts across neuronal compartments: AIR decreased synaptic activity and long-term potentiation (LTP) and impaired axonal conduction, synchronization, and action potential (AP) properties, while D-βHb rescued neuronal functions associated with axonal conduction, synchronization, and LTP.

Keywords: beta-hydroxybutyrate, GLUT4, hippocampus, insulin resistance, ketone bodies

2. **Significance statement**

This study investigates the impact of acute insulin resistance on the functionality of the hippocampal circuit and the potential protective effects of ketone body supplementation. By inhibiting GLUT4 receptors to induce acute insulin resistance, we reveal several detrimental changes caused by impaired neuronal glucose uptake. These changes include impairments in synaptic activity, axonal conduction, and neuronal firing properties. The study further examines the distinctive effects of acute insulin resistance and the rescue agent D-βHb on synaptic activity, long-term potentiation, axonal conduction, synchronization, and neuronal firing. By shedding light on neuronal responses during insulin resistance, this investigation advances our understanding of neurological disorders associated with hypometabolism and highlights the potential therapeutic value of D-βHb.

3. **Introduction**

Over the past two decades, research on insulin signaling in the brain has become increasingly important in studies of type 2 diabetes mellitus (T2DM) and Alzheimer's disease (AD) [1,2]. Insulin plays a critical role in memory formation processes in the hippocampus, and systemic insulin resistance can interfere with hippocampal metabolism and cognitive function, as shown by various studies [3,4]. Additionally, insulin is an essential element in memory processing in the hippocampus and a vital mediator of cognitive impairment in patients with T2DM and AD due to its function in promoting glucose transporter 4 (GLUT4) translocation [5,6]. Although insulin from the blood crosses the blood–brain barrier, research suggests supplementary local insulin synthesis and release in the brain [7], which enhances the pro-cognitive effects of brain glucose [8]. Therefore, impaired glucose uptake in the hippocampus may contribute to cognitive decline associated with aging, T2DM, and AD [9,10,11].

This relationship has led to the hypothesis that brain hypometabolism reflects encroaching neuronal insulin resistance [12]. The hippocampus is highly enriched with GLUT4 receptors,

which serve as the primary neuronal insulin-dependent glucose transporter, especially in brain areas with high concentrations of insulin receptors and relatively high neuronal activity [8,13,14]. Insulin acts by enhancing GLUT4 translocation across neuronal membranes under the regulation of phosphatidylinositol 3-kinase (PI3K), which promotes memory formation [15,16]. During memory formation, GLUT4 is primarily expressed in the soma rather than in the more metabolically active hippocampal neuropil [17,18], suggesting that the primary effect of insulin may be the maintenance of neuronal firing. Mouse models of AD or diet-induced obesity (DIO) showed blunting of the pro-cognitive effects of intrahippocampal insulin injections and decreased local glucose metabolism [19,20], coupled with neuronal hyperexcitability with epileptiform spikes and impairment of GLUT4 translocation [21].

During periods with lower glucose availability, ketone bodies (KBs) supplement metabolism as an alternative fuel source [22,23]. The ketogenic diet has shown pro-cognitive benefits in patients suffering from T2DM or AD. These benefits of the ketogenic diet may arise due to reduced neuronal firing rates during ketosis [24,25], increased ATP:ADP ratios [26], increased secretion of gamma-aminobutyric acid (GABA) due to substantial formation of acetyl-coenzyme A [27], equilibration of the NAD:NADH ratio, and reduced production of free radicals, which together may help to temper neuronal hyperexcitability and its metabolic consequences [28,29].

In addition, KBs are crucial in protecting mitochondria from acute metabolic stress by preventing mitochondrial permeability transition (mPT) through their effects on intracellular calcium levels [30,31]. Furthermore, KBs can affect neuronal firing by promoting the opening of ATP-sensitive K^+ channels (K-ATP), thus reducing the cytosolic pool of ATP generated from glycolysis [25,31].

Exogenous KBs, such as *D*-β-hydroxy-butyrate (D-βHb) ester, can increase KB levels in circulation without the severe dietary restrictions of the ketogenic diet [32,33]. Whether exogenous KBs maintain their neuroprotective effects in patients with normal plasma glucose levels remains unclear; however, recent studies have shown that in healthy adults, D-βHb led to increased overall brain activity and stabilized functional networks [34,35].

These observations led us to hypothesize that exogenous KBs could be utilized to rescue neuronal metabolism after cerebral insulin resistance. To test this hypothesis, we established a murine hippocampal model of acute insulin resistance (AIR) through the inhibition of GLUT4 by administration of indinavir [36,37]. We then studied how neuron-specific insulin resistance affected hippocampal neurons in the CA3-CA1 circuit, a model circuit for studying learning and memory. We tested the effects of D-βHb during AIR to determine the therapeutic potential of exogenous KBs in hypoglycemic animals. To evaluate the circuit-wide effects on synaptic and axonal function, we obtained field potential recordings in the hippocampi of the treated mice and patch-clamp recordings in hippocampal slices to assess the in vitro effects of AIR and D-βHb on the electrophysiological properties of CA1 pyramidal neurons and CA1 fast-spiking interneurons (FSIs). Finally, we used computational modeling approaches to relate our electrophysiological results and Na^+/K^+ ATPase dysfunction as the potential reason for the detrimental changes observed during AIR [38].

4. **Results**

Various paradigms of synaptic plasticity associated with learning and memory have been identified in the hippocampus. Many studies have investigated long-term potentiation (LTP), long-term depression (LTD), spike-timing-dependent plasticity, and excitatory postsynaptic potential (EPSP)-spike potentiation in hippocampal circuits, making the hippocampus a classic system for studying neuroplasticity. Furthermore, the simple cytoarchitecture of the hippocampus makes it an ideal model system. In this study, we utilized indinavir, a potent GLUT4 receptor blocker, to pharmacologically induce AIR in hippocampal slices. Our investigation focused on the stratum radiatum of CA1, where numerous synapses are formed between Schaffer collaterals (SCOs) and the apical dendrites of pyramidal neurons.

4.1 Synaptic activity and LTP, but not fiber volleys (FVs), are adversely affected by AIR and are not reversed by either 0.1 mM or 1 mM D-βHb.

To test synaptic transmission within CA1 for a wide range of energetic demands, we measured the circuit's response under 3 different stimulation paradigms. First, we applied mild physiological stimulation (not imposing high energetic demands [39,40]), consisting of paired stimulation applied at 25 Hz, repeated every 20 s over 30-60 trials [**Fig. 1A-F**].

During the AIR condition, we observed strong decreases in field excitatory postsynaptic potential (fEPSP) amplitudes, -39.23 ± 8.72% (1st stimulation) and -38.79 ± 8.93% (2nd stimulation), compared to baseline [**Fig. 1A**]. The amplitude did not recover when D-βHb was applied at low (0.1 mM) [**Fig. 1A**, +13.10 ± 6.64% and +14.07 ± 6.76%, p=0.34, p=0.30] or high (1 mM) concentrations [**Fig. 1A**, -5.98 ± 6.13% and -5.81 ± 6.26%, p=0.88; p=0.56]. No changes in the paired-pulse ratio (PPR) were observed in any of the conditions [**Fig. 1B**, Control: 1.89; AIR: 1.92; 0.1 mM D-βHb+AIR: 2.00; 1 mM D-βHb+AIR: 1.88; p=0.54], suggesting that the activity at the synaptic sites remained largely unchanged.

When applied over sufficient time, our paired stimulation triggered LTP in CA1, as evidenced by a gradual increase in the fEPSP amplitude [**Fig. 1C, top**] but no change in the PPR [**Fig. 1C, bottom**]. Therefore, we compared the LTP magnitude between the groups by calculating the ratio of the fEPSP amplitudes during the first 10 min and the amplitudes at 40 ± 10 min [**Fig. 1D-F**]. The control condition showed the strongest LTP ratio of 1.53 ± 0.13. LTP induction was almost abolished during AIR [**Fig. 1E**, 1.06 ± 0.06 ratio; -30.66 ± 9.42% reduction vs. control, p=0.018], and 0.1 mM D-βHb did not reverse this effect [**Fig. 1E**, 1.08 ± 0.08, +1.25 ± 6.61% AIR vs. D-βHb+AIR 0.1 mM, p > 0.99]; however, 1 mM D-βHb did reverse this effect [**Fig. 1E**, 1.39 ± 0.10, +21.19 ± 7.64% AIR vs. D-βHb+AIR 1 mM, p=0.044].

Moreover, we found no significant effects of either AIR or D-βHb+AIR on the amplitudes of the FVs [**Fig. 1F**, Control: 1.03 ± 0.08 mV; AIR: 0.89 ± 0.07; D-βHb+AIR 0.1 mM: 0.85 ± 0.08; D-βHb+AIR 1 mM: 1.03 ± 0.12; p=0.40]. Next, we tested whether the circuit would behave differently under a stronger stimulation that imposed greater metabolic demands. We stimulated the SCO

with 20 pulses applied at 25 Hz, with 20 s breaks between trials. To ensure that the onset of LTP did not skew the results, we recorded all train stimulations at least 40 min after the paired stimulation paradigm.

All compared groups showed potentiation of fEPSP amplitudes during the train, reaching a peak at stimuli 5-6. Thereafter, the amplitudes decreased slightly but remained potentiated [**Fig. S1A, B**]. Interestingly, throughout the entire stimulation period, the fEPSP amplitudes matched the differences we observed during the paired stimulation experiments [**Fig. S1B**; at stimulus 5: -34.25 ± 11.80% Control vs. AIR, p=0.031; -40.54 ± 11.48% Control vs. 1 mM D-βHb+AIR, p=0.000044; +3.37 ± 7.80 AIR vs. 0.1 mM D-βHb+AIR, p = 0.99; -25.21 ± 7.36% AIR vs. 1 mM D-βHb+AIR, p=0.0054]. The FV amplitudes followed a different pattern, with potentiation at stimulus 2, followed by a consistent decline to approximately 70% of the initial amplitude [**Fig. S1C**]. Similar to the paired stimulation experiments, no statistically significant differences were observed between groups at any time point during the train stimulations [**Fig. S1C**; p=0.16 to 0.40].

Finally, we examined the hippocampal circuit under intense nonphysiological stimulation conditions. This involved applying long trains of 50 stimuli at 25 Hz, spanning across 60 trials with a 20 s break between each trial. The responses during this specific stimulation condition varied among trials, making it inappropriate to average the values over the entire stimulation period. As a result, we represent the fEPSP and FV amplitudes as heatmaps. In these heatmaps, each point represents the group's mean response to a single stimulus at a given time point.

Consistent with our previous results, we observed a period of fEPSP amplitude potentiation followed by a steady decline [**Fig. S2A-D**; at maximum, trial 4-6, stimuli 7-9: -34.81 ± 10.56% Control vs. AIR, p=0.0084; -48.27 ± 11.37% Control vs. 1 mM D-βHb+AIR, p=0.00065; +10.19 ± 11.39% AIR vs. 0.1 mM D-βHb+AIR, p=0.59; -13.66 ± 9.08% AIR vs. 1 mM D-βHb+AIR]. Synaptic depression was first observed during the final stimuli of the stimulation trains, approximately 3 min into the stimulation period, and became more prominent with each subsequent train stimulation application [**Fig. S2A-D**]. In general, the fEPSP amplitudes in the control and AIR groups differed substantially during the first 7 min of the recordings [**Fig. S2A**]. The fEPSP amplitudes in the control and 1 mM D-βHb+AIR groups also differed throughout most of the stimulation trains [**Fig. S2B**], but the fEPSP amplitudes in the 0.1 mM D-βHb+AIR and AIR groups scarcely differed except at the end of the stimulation trains [**Fig. S2C**]. The fEPSPs in the AIR and 0.1 mM D-βHb groups were generally comparable. The FVs remained statistically similar among all the groups, with approximately the same response pattern [**Fig. S2E-G**], replicating the results in Fig. 1 and Fig. S1.

Taken together, these results strongly suggest that the effects of AIR and/or D-βHb could differ among cellular compartments (i.e., dendritic versus somatic) and have different specificity for various cellular compartments, with synapses being particularly susceptible to the metabolic challenges induced by GLUT4 inhibition.

4.2 AIR impairs axonal conduction speeds, but D-βHb treatment restores and enhances axonal conduction in a dose-dependent manner.

In the previous sections, we highlighted how AIR and D-βHb affected fEPSPs and FVs, finding a surprising lack of adverse effects of AIR on FV amplitudes and a noticeable reduction in fEPSP amplitudes, with the effects further exacerbated by D-βHB. This difference suggests that AIR and/or D-βHb treatment might have differential effects on cellular compartments. We then investigated whether other axonal properties changed during AIR and whether D-βHB application remedied such changes.

We found that inducing AIR resulted in a strong reduction in the conduction velocities (CVs) of SCOs [**Fig. 2C**; -13.07 ± 2.87% Control vs. AIR, p=0.027]. After the addition of 0.1 mM D-βHb during AIR, the CV recovered to control levels [**Fig. 2C**; +12.43 ± 4.42% AIR vs. 0.1 mM D-βHb+AIR, p=0.034; +0.01 ± 0.07% Control vs. 0.1 mM D-βHb+AIR, p=0.99], and the application of 1 mM D-βHb significantly improved the CV, surpassing the control level [**Fig. 2C**; +31.79 ± 4.59% for AIR vs. 1 mM D-βHb+AIR, p=4.2E-8; +19.10 ± 4.53% for control vs. 1 mM D-βHb+AIR, p=0.00057].

To better interpret these findings, we constructed a computational model of the CV by employing an approximation of axonal cable theory (see Methods). Our model examined three processes that determine the CV: the resting membrane potential (V_R), peak membrane potential (V_A, the amplitude of AP overshoot), and activation threshold potential (V_T, potential for Na_v activation). We considered V_T to be robust to various physiological conditions, as this value primarily depends on the Na_v channel type and gating kinetics [41]; therefore, we fixed V_T at a constant value of -50 mV in our calculations. We varied V_R between -90 and -60 mV and V_A between 10 and 30 mV, both of which are considered typical physiological ranges. We normalized the results according to a reference state with V_R = -75 mV, V_A = 30 mV, and V_T = -50 mV. The modeling results showed that decreased CV was associated with either hyperpolarized resting membrane potential or decreased peak action potential (AP) amplitude [**Fig. 2F-G**].

4.3 AIR adversely affects input timing, which is restored by high D-βHb concentrations.

Changes in the CV magnitude and the resulting differences in the input timing would likely desynchronize the hippocampal circuit. Therefore, we investigated whether the latency of FVs changes during stimulation with 20 pulse trains.

In all treatment groups, the early FVs showed ~-0.2 ms improvement in latency. During the first 3 min, all experimental groups were comparable and exhibited the same pattern of latency changes. Afterward, the AIR and 0.1 mM D-βHb+AIR groups displayed progressively more prominent delays than the Control group, while the Control and 1 mM D-βHb+AIR groups remained comparable. During AIR, we observed the largest delays [**Fig. 3E-F, Fig. 3I, L**; at 15 min, stim. 9-11: +2.69 ± 0.84 ms, Control vs. AIR, p=0.0077; 2.64 ± 0.94 ms, AIR vs. 1 mM D-βHb+AIR, p=0.020]. The increased delays during the stimulation suggest that the detrimental effects of AIR

are exacerbated over longer periods.

4.4 AIR increases membrane resistance (R_m) without affecting other intrinsic membrane properties of CA1 pyramidal neurons, and D-βHb treatment during AIR does not rescue R_m to normal levels.

The above results [**Fig. 2**] indicate that AIR might negatively impact the membrane properties of hippocampal neurons; therefore, we sought to identify the properties most vulnerable to AIR and test D-βHb as a recovery agent. Based on the dose–response results from the field potential studies, we selected 1 mM D-βHb for use in patch-clamp experiments, testing the effects of AIR and D-βHb on the intrinsic membrane properties of CA1 pyramidal neurons (membrane resistance, R_m; membrane capacitance, C_m, and resting membrane potential, RMP; V_{rest}) and their spike thresholds. We found that the R_m of the CA1 pyramidal neurons in the AIR group was significantly increased compared with that of the neurons in the control group [**Fig. 4B**, +43.24 ± 3.73%, p=1.41E-07], and this increased value was observed even with the application of 1 mM D-βHb [**Fig. 4B**, +27.86 ± 8.93%, p=0.030], while the results in the AIR and 1 mM D-βHb+AIR groups were similar (p=0.31). Interestingly, neither the C_m [**Fig. 4C**, 114.25 ± 9.73, 115.52 ± 9.26, 132.20 ± 9.46, Control, AIR, D-βHb+AIR, respectively, p=0.32], spike threshold [**Fig. 4E**, -46.31 ± 0.76, -44.53 ± 0.80, 44.64 ± 0.73, p=0.17] nor $V_{rest.}$ [**Fig. 4F**, -67.26 ± 1.17, -63.57 ± 1.38, -65.11 ± 0.99, p=0.093] were significantly affected by either the AIR or D-βHb+AIR treatments.

4.5 AIR increases the frequency of spontaneous excitatory postsynaptic currents (sEPSCs) at CA1 synapses and mildly increases sEPSC amplitudes. D-βHb does not reverse the increase in frequency but mildly decreases sEPSC amplitudes.

Recovering the membrane back to the resting potential during synaptic transmission is the most energy-consuming neuronal process (~% of total ATP produced [42]); therefore, we investigated changes in the frequency and magnitude of spontaneous EPSCs that might explain the ~35% decrease in fEPSP amplitudes reported above [**Figs. 1-3**].

AIR significantly increased the frequency of sEPSCs, with approximately twice as many events observed in the AIR group than in the control group [**Fig. 5A, B**; 0.53 vs. 0.96 Hz, +0.42 ± 0.12 Hz, p=0.0031]. Interestingly, D-βHb failed to rectify the increased sEPSC frequency [**Fig. 5A, B**; D-βHb+AIR 0.93 vs. AIR 0.96 Hz, 0.021 ± 0.15 Hz, p=0.99; D-βHb+AIR vs. Control, +0.40 ± 0.12 Hz, p=0.0091]. However, the amplitude, rise time, and sEPSC decay time did not differ significantly among the groups [**Fig. 5C-E**].

Given the change in R_m, the lack of significant changes in the amplitudes is surprising. Several studies utilizing different metabolic states, such as food deprivation [43] and inhibition of glycolysis [44], showed increased miniature EPSC (mEPSC)/sEPSC amplitudes; therefore, we decided to investigate the sEPSCs in more detail. In most central synapses, the distribution of mEPSC/sEPSC amplitudes shows several peaks related to the simultaneous release of multiple quanta of a neurotransmitter [45], with each subsequent peak linked to an increasing number of

concurrent sEPSCs. According to the multiplicative nature of this process, we assumed that small changes in amplitudes [**Fig. 5E**] would scale up. We detected 2-4 distinct peaks in ~85% of the analyzed cells [**Fig. S3A-C**], with no differences in the number of cells with multipeak distributions among the groups [**Fig. S3C**; 89.5% in Control; 84.2% in AIR, 87.5% in D-βHb+AIR]. In line with our initial assumptions, the scaled amplitudes revealed differences among the groups [**Fig. S3E**]: the amplitudes in the AIR group were significantly higher than those in the D-βHb+AIR group [p1: p=0.048; p2: p=0.0054; p3: p=0.0038; p4: p=0.021] and differed from those in the control group at peak 3 [p=0.007]. The Control and D-βHb+AIR groups did not show significant differences at any point [**Fig. S3E]**, despite the elevated sEPSC frequency in the D-βHb+AIR group.

We validated these findings by comparing the normalized amplitude distributions among the different groups [**Fig. S3F-I**]. Within the range correlating to peaks 2–4 (sEPSC of ~20 pA or greater), significantly more large events were observed in the AIR group (15.19% of total) than in the control (7.65%) or D-βHb+AIR (9.48%) groups [**Fig. S3F-I**], while the results in the control and D-βHb+AIR groups were essentially comparable. This result suggests that during AIR, the elevated frequency of events increased the probability of multi–vesicular events occurring, which was further exacerbated by the ~20% increase in R_m. On the other hand, D-βHb+AIR produced a distribution resembling the control, as if the vesicles had lower glutamate content, as suggested by the literature [46,47].

4.6 *AIR slightly changes the firing pattern of hippocampal pyramidal neurons and causes increased membrane depolarization with input. These effects are reversed by D-βHb, which also increases AP amplitudes.*

The action potential (AP) generation and subsequent recovery of V_m to resting levels require a large part of the energy budget of pyramidal neurons (~41% of all produced ATP [42]). Therefore, we investigated whether pyramidal neurons retain their input–output curves (I-O curve) during AIR and how D-βHb alleviates AIR effects.

First, we focused on the firing frequency [**Fig. 6A**]. Cells in the AIR group showed increased firing at lower current injections than those in the D-βHb+AIR group [**Fig. 6B**, 75–150 pA, p=0.0038 to 0.050], but with the same maximal firing rate. These results suggest that the cells activate earlier in the AIR condition than in the control or D-βHb+AIR conditions. To test this further, we measured the maximum depolarization obtained by each neuron during the final 5 ms of each current injection step [**Fig. 6D**]. AIR neurons had slightly higher depolarization with each injection step compared to control neurons [**Fig. 6E, F**; p=0.0027 to 0.048] or D-βHb+AIR [**Fig. 6E, F**; p=0.0029 to 0.042].

Next, we investigated the average AP peak amplitudes [**Fig. 6G**], per step [**Fig. 6H**]. Surprisingly, D-βHb+AIR neurons showed larger amplitudes, which were consistently elevated throughout the injection period, than control or AIR neurons, while AIR neurons remained comparable to control neurons [**Fig. 6I**, p=0.0017 to 0.036, AIR vs. Control; p=0.0093 to 0.044, AIR vs. 1 mM D-

βHb+AIR].

4.7 *AIR increases the AP decay time, while D-βHb accelerates the AP rise time without reversing the AIR-induced slower AP decay.*

We next proceeded to investigate other AP properties: the decay time (from the overshoot peak to 0 mV) [**Fig. 7A-C**] and rise time (from 0 mV to the overshoot peak) [**Fig. 7D-F**]. We found that control neurons had significantly lower average AP decay times than AIR [**Fig. 7B, C**; p=0.047 to 0.0019] and D-βHb+AIR neurons [**Fig. 7B, C**; p=0.041 to 0.0023] for almost all current injection steps. Moreover, AIR and D-βHb+AIR cells did not significantly differ at any point [**Fig. 7B, C**; p=0.32 to 0.99]. D-βHb+AIR cells demonstrated faster rise times than control cells [**Fig. 7E, F**; p=0.000094 to 0.0025] and AIR cells [**Fig. 6E, F**; p=0.047 to 0.0052] for most injection steps. Interestingly, AIR cells exhibited slightly faster AP rise times exclusively at the lowest current injection times [**Fig. 4N, O**; p=0.012 to 0.035]. These slightly faster APs were likely due to earlier activation of the cells, as shown in [**Fig. 6B-C, E-F**].

Finally, as we did not observe significant differences in the firing frequency among the groups [**Fig. 6B, C**], we examined variations in the timing of AP firing based on the intervals between consecutive APs (AP interevent interval, AP IEI) [**Fig. 7G**], but we did not observe obvious changes in the AP IEI [**Fig. 7H, I].**

4.8 *AP adaptation is impaired during AIR, with AP amplitudes showing steeper declines, and is not reversed by D-βHb.*

The AP overshoot amplitudes, decay times, and rise times demonstrated steeper slopes in the AIR and D-βHb+AIR groups than in the control group. The AP properties during neuronal firing undergo dynamic changes [48], commonly referred to as spike adaptation or spike-frequency adaptation [48], and in our experiments, we observed that GLUT4 antagonism intensified these changes.

To test this observation, we compared the peak amplitudes of the first APs [**Fig. S4A-D**], the averaged APs [**Fig. 6G-I**, **Fig. S4E**] and the final APs during current injections [**Fig. S4F**]. The first APs represent neuronal firing after rest (10 s between subsequent injections), while the average and final APs represent firing after energy expenditure. As expected, the first APs displayed minimal changes in amplitude during injections [**Fig. S4D**], with larger amplitudes observed in the D-βHb+AIR group than in the control group. Moreover, although elevated amplitudes were observed in the AIR group, the results did not differ significantly from those in the control or D-βHb+AIR groups. For the final APs, we observed a sharp decline in amplitude, which scaled with the injected current [**Fig. S4F**], in both the AIR and D-βHb+AIR groups. Lower amplitudes were observed in the control group than in the D-βHb+AIR group for 100-300 pA injections (p=0.040 to p=6E-05), and the results remained comparable to those in the AIR group until the final, large, 400-500 pA injections (p=0.032 to p=0.0011), when the APs in the AIR group decreased significantly [**Fig. S4F**]. The results in the AIR and D-βHb+AIR groups remained

328 consistently different. Linear fits to the average AP amplitudes revealed significantly steeper
329 declines in the AIR and D-βHb+AIR groups [**Fig. S4G, H**; p=0.00039, AIR vs. Control; p=0.0012,
330 D-βHb+AIR vs. Control], indicating that prolonged neuronal activity is heavily affected by AIR and
331 D-βHb does not provide direct recovery.

332 4.9 *Changes in AP decay and rise times correspond to differences in the widths of FVs.*

333 In our initial analysis of the field potential data, we focused on the amplitudes of the biological
334 signals. Consistently, we found no significant changes in the FV amplitudes [**Figs. 1F, 2C, 3E-G**],
335 which supports our findings on AP overshoot amplitudes [**Fig. 6G-I**] (except in the D-βHb+AIR
336 group). Based on these results, we investigated whether the changes in the AP decay and rise
337 times corresponded to changes in the FV widths during train stimulation [**Fig. S5**].

338 Consistent with our findings on AP decay/rise times [**Fig. 7A-F**], the widest FVs during the
339 stimulation were consistently observed in the AIR group, followed by the control group, with the
340 narrowest FVs observed in the 1 mM D-βHb+AIR group [**Fig. S5D**]. We found differences between
341 the AIR and control groups (p=3.94E-06 to 0.049) and AIR and 1 mM D-βHb+AIR groups
342 (p=4.04E-05 to 0.046) throughout the whole stimulation period, while the results in the control and
343 1 mM D-βHb+AIR groups were not different (p=0.079 to 0.99), supporting our AP decay/rise time
344 findings [**Fig. 6G-I**].

345 4.10 *With abolished GABAergic inhibition, AIR strongly decreased the firing rates of CA1*
346 *pyramidal neurons and FSIs, which were not rescued by D-βHb.*

347 We next investigated the properties of CA1 pyramidal neurons and FSIs after pharmacologically
348 abolishing AMPA/kainate excitatory (2,3-dioxo-6-nitro-7-sulfamoyl-benzo-quinoxaline; NBQX)
349 and fast GABAergic inhibitory (gabazine) transmission [**Fig. S6**].

350 We first recorded the firing frequency of CA1 pyramidal neurons [**Fig. S6A, B**] at different
351 activation levels [**Fig. S6C, D**] and found that AIR prominently decreased their firing rate when
352 compared with the control [**Fig. S6C**, p=0.024 to 0.0053]. Surprisingly, the application of 1 mM D-
353 βHb during AIR resulted in a stronger reduction in the firing rate than in the control group [**Fig.**
354 **S6E**, p=0.000027 to 0.035]. The AIR and D-βHb+AIR results remained similar throughout the
355 injections [**Fig. S6E**]. However, all groups differed significantly with respect to the maximum firing
356 rate, with the highest firing rate observed in the control group (31.03 ± 3.43) and the lowest firing
357 rate observed in the D-βHb+AIR group (13.17 ± 2.05).

358 Next, we examined CA1 FSIs using the same drug conditions [**Fig. S6E, F**]: AIR decreased the
359 firing rate of FSIs compared with the control [**Fig. S6G**, p=0.012 to 0.048], which was not reversed
360 by D-βHb [**Fig. S6H**, p=0.00017 to 0.035]. For pyramidal neurons, the FSIs in the AIR and D-
361 βHb+AIR groups remained mostly comparable [**Fig. S6G**]. None of the groups differed in the
362 maximum firing rate [**Fig. S6H**, p=0.068].

363 4.11 The *Hodgkin-Huxley model predicts that impairments in Na^+/K^+ ATPase activity result in*
364 *more depolarized V_{rest}, lower AP overshoot (V_a), and increased neuronal firing.*

365 Here, we aim to explain the previous observations of dysregulated firing dynamics in response to
366 AIR. We hypothesize that indinavir restricts the energy supply of neurons and thus impairs the
367 neuronal Na^+/K^+ ATPase. To test this hypothesis, we developed a computational model of an
368 isolated CA1 neuron in the absence of inhibition and toggled Na^+/K^+ ATPase activity through the
369 enzyme kinetic parameter v_{ATPase}^{max} (see Supplementary Methods, **Fig. S7**). **Fig. S7A, B** (at two
370 different temporal scales) shows the predicted changes in neuronal firing dynamics when the
371 Na^+/K^+ ATPase is impaired. This impairment predicted the depolarization of the resting membrane
372 potential [**Fig. S7C**] and is consistent with the trends of our I/O curves [**Fig. 4F**]. Furthermore, in
373 this depolarization model, the magnitude of the membrane potential shift needed for an AP is
374 reduced. Consequently, the model predicted increased firing frequency [**Fig. S7D**]. Finally, the
375 model predicted that the Na^+/K^+ ATPase should act more slowly to recover ion gradients after an
376 AP, causing the amplitudes of the subsequent APs to decline progressively with time [**Fig. S7E,**
377 **F**]. This amplitude decrease is consistent with the trends in the measured CV [**Fig. 2**].

378 5. **Discussion**

379 Central insulin resistance impairs cognitive performance and promotes hippocampal
380 neurodegeneration and memory loss [49,50]. Our present results highlight the adverse effects of
381 GLUT4 inhibition on synaptic function and LTP, in accord with findings that acute and chronic
382 blockade of GLUT4 are detrimental to hippocampus-mediated memory tasks, thus suggesting
383 that GLUT4 is critical for the acquisition and consolidation of memory [8,14]. Memory formation
384 promotes GLUT4 incorporation into the membrane, resulting in increased glucose flux into
385 neurons [14,51]. This process enables increased metabolic support during high-demand
386 activities. Crucially, most GLUT4s localize in the perikaryon [52,53], likely near axosomatic
387 synapses, which are associated with synaptic plasticity and long-term memory (LTM). Indeed,
388 prolonged blockade of GLUT4 glucose transporters in the brain results in impaired formation of
389 LTM [14] and decreased levels of hippocampal brain–derived neurotrophic factor (BDNF) [54].
390 Moreover, hypoglycemia negatively affects memory performance and cognition [55,56; however,
391 see 14].

392 In this study, we found that AIR increased the frequency of sEPSC events, a finding which is
393 consistent with previously published data showing similar increases during food deprivation [44],
394 inhibition of glycolysis [43] and ischemia [57], likely due to hypoglycemia-driven Ca^{2+}
395 accumulation at presynaptic terminals [43,57]. These studies also suggest that presynaptic
396 glycolysis is essential for maintaining synaptic transmission, even at low frequencies, and that
397 mitochondrial respiration cannot compensate for these effects [43,57]. Normally, glycolysis
398 requires approximately one-third of the energy used at presynaptic terminals, thus sustaining low-
399 frequency transmission. In addition, impaired glycolysis leads to slower, broader, and smaller AP
400 waveforms and depolarization of the resting membrane potential [44], which is consistent with our
401 results. Interestingly, D-βHb+AIR treatment, which showed the same increase in the frequency of

402 sEPSC events as AIR, led to the lowest sEPSC amplitudes [**Fig. S3E**]. This result suggests a
403 reduction in the number of synaptic vesicles and is consistent with reports of reduced conversion
404 of glutamate to aspartate during ketosis [46,47].

405 Although the results of our computational models are consistent with the observed changes in the
406 resting-state membrane potential and firing frequency during AIR, there were seemingly
407 contradicting results with respect to the AP peak amplitude. Specifically, we found no significant
408 changes in the average AP overshoot amplitudes during AIR, and our model predicted a decrease
409 due to energy constraints. In the model, we did not consider a progressive decline in available
410 energy, which is suggested by the steeper AP adaptation [**Fig. S4**]. Moreover, neurons may
411 compensate for such energetic limitations by increasing R_m (as reported in 44), while our model
412 assumes that R_m remains unchanged. When those factors are accounted for, the model and
413 experimental data agree: during periods of extensive activity, energy reserves in neurons are
414 progressively depleted and, provided that the neuron rapidly fires multiple APs, the negative
415 effects of hypoglycemia overcome compensatory R_m increases; then, the AP amplitudes
416 decrease below control levels [**Fig. S4**]. Furthermore, we used the maximal Na^+/K^+ ATPase
417 activity to represent ATP availability and considered literature estimates of kinetic and
418 thermodynamic rate constants. A more direct approach might consider ATP concentration as an
419 input variable, in cases in which such experimental data are available.

420 Our model aims to establish the underlying causes of the changes in CV, and we investigated
421 V_{rest} and AP peak amplitude as two critical factors. The model explains CV recovery and CV
422 increases during D-βHb+AIR treatment, as the measured AP peak amplitudes remain consistently
423 elevated and V_{rest} changes are negligible, but fails in the case of AIR alone, with the AP amplitudes
424 remaining comparable to the control levels and V_{rest} tending to depolarize. This discrepancy might
425 reflect the simplistic nature of our model, which neglects complex ion dynamics, altered
426 membrane permeability and synaptic processes.

427 The ketogenic diet has been used to treat epilepsy for decades and has been considered in many
428 therapeutic applications [32]. Possible mechanisms include modulation of ATP-sensitive K^+
429 channels (K_{ATP}), free fatty acid receptor 3 (FFAR3/GPR41) activation, promotion of GABA
430 synthesis, and epigenetic modifications [58]. The action of D-βHb in modulating potassium flux
431 through K_{ATP} channels may be most relevant in the present context [59] since K_{ATP} activation
432 results in decreased neuronal firing rates [60,61] and prevents picrotoxin-induced epileptiform
433 activity in the hippocampus [62]; thus, this action may explain the present findings that firing rates
434 and membrane depolarization remained at control levels in the presence of 1 mM D-βHb during
435 AIR (despite elevated R_m).

436 D-βHb is a precursor of glutamine, which promotes increased GABA levels, as seen in studies on
437 the ketogenic diet in patients with epilepsy [63]. D-βHb also directs glutamate toward GABA
438 production by reducing the conversion of glutamate to aspartate [46,47]. In addition, D-βHb
439 directly affects the vesicular glutamate transporter 2 (VGLUT2) by inhibiting Cl^- dependent
440 glutamate uptake. VGLUT2 is critical for glutamate excitatory transmission in CA3-CA1 [64], and

441 conditional VGLUT2 knockout results in impaired spatial learning and reduced LTP [64]. Together
442 with the increased formation of GABA and/or GABA derivatives, VGLUT2 inhibition could reduce
443 glutamate excitatory transmission [65].

444 The present results have important implications for the treatment of conditions such as type 2
445 diabetes, metabolic syndrome, and seizure disorders that involve insulin hyposensitivity.
446 According to NIH estimates, ~38% of Americans display symptoms of prediabetes [66], and this
447 percentage is expected to increase. With longer average lifespans and demographic changes
448 leading to an increase in the aging population, obtaining insights into the outcomes of metabolic
449 dysfunction and its potential treatment has become a crucial issue. Our results provide unique
450 insight into the potential use of KBs as an inexpensive and relatively risk-free treatment for
451 metabolic disorders and insulin resistance. Medical researchers can use this information to
452 discover new targets for treatment and develop more effective therapies. Further research in this
453 area could inform novel treatment approaches that address the complex effects of metabolic
454 disorders on brain health.

455 6. **Materials and Methods**

456 6.0 *Mice.*

457 Breeding pairs of transgenic GAD2Cre/GCamp5gTdTomato, Thy1/GCamp6fTdTomato, and
458 C57BL/6J mice were originally obtained from The Jackson Laboratory (stocks 010802, 024477,
459 024339) or Charles River Laboratories and bred in-house under standard conditions of a 12-12
460 hour light-dark cycle, with food and water available *ad libitum*. The University of Rochester School
461 of Medicine and Dentistry Institutional Animal Care and Use Committee approved all experiments.
462 Mice of both sexes aged between 30 and 60 days (P30-P60) were used in all experiments.

463 6.1 *Electrophysiology – slice preparation.*

464 Coronal brain slices containing the hippocampus were used in all recordings. Mice were deeply
465 anesthetized with a mixture of isoflurane and air (3% v/v) and decapitated, and their brains were
466 extracted and cut using a Leica VT1200S vibratome into 300 µm-thick slices in ice-cold ACSF
467 solution containing (in mM): 230 sucrose, 1 KCl, 0.5 $CaCl_2$, 10 $MgSO_4$, $NaHCO_3$, 1.25 NaH_2PO_4,
468 0.04 Na-ascorbate, and 10 glucose; 310 ± 5 mOsm, pH adjusted to 7.35 ± 5 with HCl, and gassed
469 with carbogen (95% O_2, 5% CO_2) for at least 30 min before use. The slices were then transferred
470 to a BSC-PC submerged slice chamber (Harvard Apparatus, USA) filled with artificial
471 cerebrospinal fluid (ACSF) containing (in mM): 124 NaCl, 2.5 KCl, 2 $CaCl_2$, 2 $MgSO_4$, 26 $NaHCO_3$,
472 1.25 NaH_2PO_4, 0.04 Na-ascorbate, and 10 glucose; 305 ± 5 mOsm/kg, pH adjusted to 7.35 ± 0.05
473 mOsm/kg, gassed with carbogen and prewarmed to 32 °C. The slices were allowed to recover in
474 warm ACSF for 15 min; then, the heating was switched off, and the chamber was gradually cooled
475 to room temperature (RT; 23 ± 2 °C) over 45 min.

476 Following recovery, individual slices were transferred to another BSC-PC chamber filled with

477 gassed ACSF and a mixture of drugs (indinavir 0.1 mM; indinavir 0.1 mM and either 0.1- or 1-mM
478 D-βHb), where they were incubated for 60 ± 15 min. Next, the slices were transferred to a
479 submerged recording chamber mounted on an upright microscope stage (E600FN, Nikon, Japan)
480 equipped with infrared differential interference contrast (IR-DIC) filters. The slices were kept at
481 RT and superfused continuously with gassed ACSF delivered by a peristaltic pump at a steady
482 rate of ~2 ml/min.

483 6.2 *Field potential recordings.*

484 Evoked field potential responses were triggered with an isolated pulse stimulator (Model 2100,
485 AM Systems, USA) using a CBARC75 concentric bipolar electrode (FHC, USA) placed between
486 CA3 and CA1. The recording electrode was placed 300 ± µm away from the stimulation electrode
487 for the CA1 FV and fEPSP recordings. During the axonal conduction velocity (CV) recordings, the
488 electrodes were spaced 300 to 900 ± 50 µm apart, and up to 6 different sites were recorded. All
489 stimulation paradigms were applied every 20 s as biphasic rectangular pulses with a total duration
490 of 240 µs, 50 ± 5 V strength (~60 ± 10% of the maximum response size), and a between-stimuli
491 frequency of 25 Hz (40 ms).

492 During non-CV recordings, three different types of stimulation were applied: paired, 20 stimuli,
493 and stimuli trains, repeated every 20 s for a total period of 20 min in each case. After each train
494 stimulation, the slice was allowed to recover for 20 min under paired stimulation conditions.

495 Recording pipettes were pulled from borosilicate glass capillaries (ID 0.86, OD 1.5, BF1-86-10,
496 Sutter Instruments, USA) with a vertical PC-100 puller (Narishige, Japan) and filled with 6% NaCl
497 (in H_2O, 1.02 M). Only pipettes with a resistance of 0.2-1.0 MΩ were used. Recording pipettes
498 were allowed to rest at the recording site for 10 min to equilibrate before the start of a recording.
499 All recorded signals were acquired using a MultiClamp 700B amplifier (Molecular Devices, USA),
500 Bessel-filtered at 2 kHz, and digitized at a sampling frequency of 10 kHz using an Axon Digidata
501 1440A digitizer (Molecular Devices, USA).

502 6.3 *Whole-cell patch-clamp recordings.*

503 Pyramidal neurons in the hippocampal CA1 region were selected for recordings based on their
504 general morphology and position within the pyramidal layer. As an additional verification, recorded
505 cells were screened for glutamate decarboxylase 2 (GAD2) $^{+}$-driven tdTomato fluorescence. Cells
506 that displayed any level of tdTomato fluorescence were rejected.

507 Patch pipettes were pulled from borosilicate glass capillaries (BF1-86-10, Sutter Instruments,
508 USA) with a vertical puller (PC100, Narishige, Japan). Pipettes had a resistance of 6–8 MΩ when
509 filled with an internal solution containing (in mM): 136 K-gluconate, 4 disodium adenosine 5′-
510 triphosphate (Na_2ATP), 2 $MgCl_2$, 0.2 ethylene glycol-bis(β-aminoethyl ether)-N,N,N′,N′-tetraacetic
511 acid (EGTA), 10 4-(2-hydroxyethyl)-1-piperazineethanesulfonic acid (HEPES), 4 KCl, 7 di(tris)
512 creatine phosphate, 0.3 trisodium guanosine 5'-triphosphate (Na_3GTP); 280–290 ± 5 mOsm/kg,

513 titrated to pH 7.3 ± 0.05 with KOH.

514 During the voltage clamp (VC) recordings, cells were clamped at a holding potential (V_h) of −70
515 mV with a Multiclamp 700B amplifier (Molecular Devices, USA). The liquid junction potential was
516 not corrected. The pipette capacitance was compensated for in all recordings. During VC
517 experiments, the series resistance (R_s) was not compensated. During the current clamp (CC)
518 recordings, a holding current was applied to the cells to maintain the membrane potential at V_h =
519 -70 ± 3 mV. All cells were bridge-balanced at 50 % of R_s. The cell capacitance was not
520 compensated for in either mode. Immediately after establishing the whole-cell configuration, the
521 cell was kept in I=0 mode to monitor V_{rest} over a period of ~120 to 180 s. The average value of
522 V_{rest} over this period is reported as the neuron's V_{rest}.

523 During the recordings, every 5 to 10 min, a series of 10 square voltage steps of −10 mV was
524 applied to monitor changes in R_s (holding voltage; V_h = -70 mV). All whole-cell currents in
525 response to voltage steps were low-pass filtered at 10 kHz with a Bessel filter and sampled at 20
526 kHz frequency (Axon Digidata 15B, Molecular Devices, USA). For inclusion in the final dataset,
527 recordings had to meet 3 criteria: 1) The R_s value after any recording protocol could not be more
528 than 20% larger than the R_s value before the protocol; 2) the R_s value during any of the recording
529 protocols could not exceed 30 MΩ; and 3) the offset drift by the end of the recordings could not
530 be higher than ± 5 mV.

531 sEPSCs were recorded in VC at V_h = -70 mV, in a single, continuous sweep for 10 to 15 min, low-
532 pass filtered at 2 kHz with a Bessel filter and sampled at 10 kHz frequency.

533 To establish the spiking threshold, each neuron was current-clamped at V_h ~ -70 ± 3 mV and
534 subjected to a ramp-shaped 200-500 pA current injection with a 1 s duration. The spike threshold
535 was determined as the membrane potential at which the first fully developed AP was visible. Each
536 ramp injection was repeated 10x, and the averaged threshold value is reported for the neuron.

537 To establish the firing properties of the recorded neurons, each neuron was current-clamped as
538 described previously and subjected to a series of square current injections with a change of 25
539 pA per step to a maximum of 0 pA, with each step having a 1 s duration and an interstep interval
540 (ISI) of 10 s. If necessary, the holding current was corrected during the protocol to maintain V_h at
541 ~ -70 ± 3 mV. During analyses, only fully formed APs that crossed the 0 mV threshold were
542 included.

543 All data acquisition was performed using pCLAMP software (Molecular Devices, USA).

544 6.4 *Field potential recordings – analyses.*

545 During field potential recordings, the biologically relevant signals are superimposed onto the
546 decaying stimulation artifact. To isolate the stimulation artifacts for subtraction from the signal at
547 the end of each recording, we applied 1 μM tetrodotoxin (TTX) to the slice and recorded 30
548 repetitions of each stimulation paradigm in the presence of TTX.

549 Recorded traces were analyzed in Igor Pro (Wavemetrics, USA). First, an average of the traces
550 recorded with TTX was subtracted from each trace. The traces were then filtered using a rolling
551 five-point average to remove noise, and the baseline was adjusted to the 1 s period before the
552 stimuli. The amplitudes and latencies of the FVs and fEPSPs were measured at their peaks.
553 Amplitudes were measured against 0 mV baselines, while latencies were measured against the
554 onset of the stimulation. During high-frequency stimulation, cells often do not have sufficient time
555 to fully recover their membrane potentials before the next stimulus is applied, leading to a gradual
556 shift in the baseline; therefore, as a correction, we subtracted the median voltage at +35 to +40
557 ms after each stimulus from each FV or fEPSP amplitude. FV widths were measured at the peaks
558 of positive deflections in the waveform, with the first peak after the artifact subtraction and the
559 second peak directly before the fEPSP.

560 All traces were screened for occasional electrical interference, and the affected data points were
561 manually removed from the analysis.

562 To measure the axonal conduction velocity (CV), we calculated the time shift (Δt, ms) between
563 the stimulus start and the time of the FV peak. Next, the linear distance between the recording
564 site and the stimulation electrode was divided by the measured Δt. We recorded CV values at 3-
565 6 sites over a span of 300-900 μm, with ~1 μm steps between sites. Each CV recording site
566 served as a replicate for statistical analysis (see Statistics). During CV recording, the stimulation
567 site remained stationary, and the sites were recorded in randomized order.

568 To calculate changes in the FV peak latency during train stimulations, the median Δt for stimuli 1-
569 3 and traces 1-2 (Δt_N) was subtracted from each Δt (normalization).

570 6.5 *Whole-cell patch-clamp – sEPSC analyses.*

571 sEPSC detection was automatized using a convolution-based algorithm in Fbrain 3.03 [67], a
572 customized program in Igor Pro 6 (WaveMetrics, Lake Oswego, USA), kindly provided by the
573 Peter Jonas Lab (IST, Klosterneuburg, Austria). Recorded traces were smoothed by subtracting
574 a 20-term polynomial fitted to the trace and digital notch (60 ± 0.5 Hz) filtered in FBrain before the
575 analysis. The convolved trace was passed through a digital bandpass filter at 0.001 to 200 Hz.
576 The event detection template had a rise-time constant τ = 1.5 ms, a decay τ = 6 ms, and an
577 amplitude of −10 pA. The event detection threshold (θ) was set to 4.2 times the standard deviation
578 of a Gaussian function fitted to the all-point histogram of the convolved trace. All events detected
579 by the algorithm were inspected visually. Events that clearly did not show the fast rise times and
580 exponential decay kinetics of a typical hippocampal EPSC were manually removed. Only cells
581 with a rejection ratio lower than 20% were included in the analysis. The analysis was performed
582 using custom-written macros provided by Dr. Maria Kukley (Achucarro Basque Center for
583 Neuroscience, Bilbao, Spain).

584 Afterwards, individual sEPSC waveforms were extracted from the trace. Each waveform
585 consisted of a 5 ms segment of the trace before the onset of the sEPSC and a 50 ms segment

586 after the sEPSC onset to capture the full decay of the waveform. Before averaging, all sEPSCs
587 were baseline-adjusted to the pre-onset time by 5 ms. The peak amplitude, 20-80% onset-to-peak
588 rise time, and decay constant τ were measured for the averaged sEPSCs. The decay constant τ
589 was calculated from the monoexponential fit from the sEPSC peak to the final ms of the averaged
590 waveform.

591 To avoid selection bias during sEPSC extraction, we repeated the Fbrain analysis at least twice
592 for each cell and averaged the results.

593 6.6 *Statistics.*

594 All data were acquired in randomized sequences, with a maximum of 2 slices (field potential
595 recordings) or 2 cells (patch-clamp recordings) from a single animal per experimental condition
596 to avoid pseudoreplication. All experimental groups had comparable distributions of ages (close
597 to P50 ± 6) and sex. The order of slice preincubation with drugs was randomized for each animal.
598 The numbers of slices or cells and animals used in each experiment are indicated in the figure
599 legends.

600 Statistical analysis was performed using GraphPad Prism 9.5.1 (GraphPad Software, USA).
601 Significant outliers were removed with the Prism ROUT method at Q = 5%, and the normality of
602 residuals and homoscedasticity were tested for each comparison. If the datasets had normal
603 residuals and equal variances, we used ordinary one-way ANOVA with *post hoc* Holm-Šídák's
604 test. If the datasets had normal residuals but unequal variances, we used Brown-Forsythe
605 ANOVA with *post hoc* Dunnett's T3 test. If the datasets were not normally distributed but had
606 equal variances, we used Kruskal-Wallis ANOVA with *post hoc* Dunn's test. In rare cases where
607 the data were neither normally distributed nor had equal variance, we applied Brown-Forsythe
608 ANOVA with *post hoc* Dunnett's T3 test. If the dataset consisted of multiple replicates, we used
609 nested one-way ANOVA with *post hoc* Holm-Šídák's test. The tested groups and p values are
610 indicated in the text or the figure legends. Individual cells or slices are labeled n, replicates are
611 labeled m, and the numbers of animals used are labeled N. If the groups tested are different, we
612 report the p values of *post hoc* tests but omit the p value of the omnibus test. If the groups did not
613 test as different, only the p value of the omnibus test is reported. For scatter plots, each point
614 represents an individual data point (cell, slice, or replicate), and the horizontal bars represent the
615 group mean ± SEM. In all other graphs, we present the mean ± SEM. The heatmaps represent
616 the group means.

617 7. **Acknowledgments**

618 We thank Dr. Vittorio Gallo (Children's National Research Institute, USA) for sharing his
619 electrophysiology setup, without which this work would not have been possible; Dr. Kieran Clarke
620 (University of Oxford) for providing D-βHb ester and advice; Dr. Joseph Abbah (Children's
621 National Research Institute, USA) for help during the preliminary stage of the research; Dr.
622 Richard L. Veech and Dr. M. Todd King (Lab of Metabolic Control, NIH/NIAAA, USA) for providing
623 D-βHb ester and advice; Dr. Ting-Jiun Chen (Mt. Sinai Medical Center, USA) for help and advice

with setting up the patch-clamp recordings; Dr. Peter Jonas (Institute of Science and Technology Austria, Austria) for providing the FBrain software; Dr Fernando Fernandez (Boston University, USA) for comments on the first draft of the manuscript; Dr Paul Hruz (Washington University School of Medicine in St. Louis, USA) for help with establishing the GluT4 inhibition model; Dr Nandkishore Prakash and Dave Saxon (Children's National Research Institute, USA) for advice and discussions; Dr Heidi Matos Galicia (National Institute of Neurological Disorders and Stroke, USA) for advice; Dr. Paul Cumming (Bern University Hospital) for critical reading of the manuscript; and members of the Mujica-Parodi laboratory (LCNeuro, USA) for discussions; C.W. also acknowledges support from the Marie-Josée Kravis Fellowship in Quantitative Biology.
This manuscript was posted on a preprint:
https://www.biorxiv.org/content/10.1101/2023.08.23.554428v3

8. **Funding**

This work was supported by the National Institutes of Health Grant K01NS110981 to N.A.S., the National Science Foundation NSF1926781 to L.M.P. and N.A.S., and the Department of Defense ARO W911NF2410047 to N.A.S.

9. **Contributions**

Conceptualization: BK, BA, CW, LMP, NAS

Methodology: BK, BA, FG, AB, JMH, CW, MK, LMP, NAS

Software: FG, AB, JMH, BA, CW, MK

Validation: BK, BA, CW, LMP, NAS

Formal Analysis: BK, BA, CW, FG, AB, JMH

Investigation: BK, BA, CW, FG, AB, JMH, LMP, NAS

Writing – Original Draft: BK

Writing – Review & Editing: BK, BA, CW, FG, AB, VV, JMH, MK, LMP, NAS

Visualization: BK, BA

Supervision: LMP, NAS

Funding Acquisition: LMP, NAS

10. **Conflicts of interest**

The authors declare no conflicts of interest.

11. **Data and materials availability**

All Data and Data tables with all analyses and tables with statistics are available at Dryad: https://datadryad.org/stash/share/XnKk8GOJq2V3Frm_KJ3BGkg7rf6P9RZRnnQlW4X5Qso. All code is available on GitHub by following the links provided in the text.

12. **References**

1. de la Monte SM. Insulin Resistance and Neurodegeneration: Progress Towards the Development of New Therapeutics for Alzheimer's Disease. Drugs. 2017;77(1):47-65. doi:10.1007/s40265-016-0674-0

2. De Felice FG, Ferreira ST. Inflammation, defective insulin signaling, and mitochondrial dysfunction as common molecular denominators connecting type 2 diabetes to Alzheimer disease. Diabetes. 2014;63(7):2262-2272. doi:10.2337/db13-1954

3. McNay EC, Recknagel AK. Brain insulin signaling: a key component of cognitive processes and a potential basis for cognitive impairment in type 2 diabetes. Neurobiol Learn Mem. 2011;96(3):432-442. doi:10.1016/j.nlm.2011.08.005

4. Zhao WQ, Chen H, Quon MJ, Alkon DL. Insulin and the insulin receptor in experimental models of learning and memory. Eur J Pharmacol. 2004;490(1-3):71-81. doi:10.1016/j.ejphar.2004.02.045

5. Kyrtata N, Emsley HCA, Sparasci O, Parkes LM, Dickie BR. A Systematic Review of Glucose Transport Alterations in Alzheimer's Disease. Front Neurosci. 2021;15:626636. Published 2021 May 20. doi:10.3389/fnins.2021.626636

6. Ghasemi R, Haeri A, Dargahi L, Mohamed Z, Ahmadiani A. Insulin in the brain: sources, localization and functions. Mol Neurobiol. 2013;47(1):145-171. doi:10.1007/s12035-012-8339-9

7. Kuwabara T, Kagalwala MN, Onuma Y, et al. Insulin biosynthesis in neuronal progenitors derived from adult hippocampus and the olfactory bulb. EMBO Mol Med. 2011;3(12):742-754. doi:10.1002/emmm.201100177

8. McNay EC, Pearson-Leary J. GluT4: A central player in hippocampal memory and brain insulin resistance. Exp Neurol. 2020;323:113076. doi:10.1016/j.expneurol.2019.113076

9. Craft S. Insulin resistance syndrome and Alzheimer's disease: age- and obesity-related effects on memory, amyloid, and inflammation. Neurobiol Aging. 2005;26 Suppl 1:65-69. doi:10.1016/j.neurobiolaging.2005.08.021

10. Kerti L, Witte AV, Winkler A, Grittner U, Rujescu D, Flöel A. Higher glucose levels associated with lower memory and reduced hippocampal microstructure. Neurology.

685 2013;81(20):1746-1752. doi:10.1212/01.wnl.0000435561.00234.ee

686 11. Antal B, McMahon LP, Sultan SF, et al. Type 2 diabetes mellitus accelerates brain aging
687 and cognitive decline: Complementary findings from UK Biobank and meta-analyses. Elife.
688 2022;11:e73138. Published 2022 May 24. doi:10.7554/eLife.73138

689 12. Zilberter Y, Zilberter M. The vicious circle of hypometabolism in neurodegenerative
690 diseases: Ways and mechanisms of metabolic correction. J Neurosci Res. 2017;95(11):2217-
691 2235. doi:10.1002/jnr.2406413. McEwen BS, Reagan LP. Glucose transporter expression in
692 the central nervous system: relationship to synaptic function. Eur J Pharmacol. 2004;490(1-3):13-
693 24. doi:10.1016/j.ejphar.2004.02.041

694 14. Pearson-Leary J, McNay EC. Novel Roles for the Insulin-Regulated Glucose Transporter-
695 4 in Hippocampally Dependent Memory. J Neurosci. 2016;36(47):11851-11864.
696 doi:10.1523/JNEUROSCI.1700-16.2016

697 15. McNay EC, Fries TM, Gold PE. Decreases in rat extracellular hippocampal glucose
698 concentration associated with cognitive demand during a spatial task. Proc Natl Acad Sci U S A.
699 2000;97(6):2881-2885. doi:10.1073/pnas.0583697

700 16. Grillo CA, Piroli GG, Hendry RM, Reagan LP. Insulin-stimulated translocation of GLUT4
701 to the plasma membrane in rat hippocampus is PI3-kinase dependent. Brain Res. 2009;1296:35-
702 45. doi:10.1016/j.brainres.2009.08.005

703 17. Stranahan AM, Norman ED, Lee K, et al. Diet-induced insulin resistance impairs
704 hippocampal synaptic plasticity and cognition in middle-aged rats. Hippocampus.
705 2008;18(11):1085-1088. doi:10.1002/hipo.20470

706 18. Ashrafi G, Wu Z, Farrell RJ, Ryan TA. GLUT4 Mobilization Supports Energetic Demands
707 of Active Synapses. Neuron. 2017;93(3):606-615.e3. doi:10.1016/j.neuron.2016.12.020

708 19. De Felice FG, Ferreira ST. Inflammation, defective insulin signaling, and mitochondrial
709 dysfunction as common molecular denominators connecting type 2 diabetes to Alzheimer
710 disease. Diabetes. 2014;63(7):2262-2272. doi:10.2337/db13-1954

711 20. Kothari V, Luo Y, Tornabene T, et al. High fat diet induces brain insulin resistance and
712 cognitive impairment in mice. Biochim Biophys Acta Mol Basis Dis. 2017;1863(2):499-8.
713 doi:10.1016/j.bbadis.2016.10.006

714 21. Martínez-François JR, Fernández-Agüera MC, Nathwani N, et al. BAD and KATP
715 channels regulate neuron excitability and epileptiform activity. Elife. 2018;7:e32721. Published
716 2018 Jan 25. doi:10.7554/eLife.32721

717 22. Kashiwaya Y, Takeshima T, Mori N, Nakashima K, Clarke K, Veech RL. D-beta-

718 hydroxybutyrate protects neurons in models of Alzheimer's and Parkinson's disease. Proc Natl
719 Acad Sci U S A. 2000;97(10):5440-5444. doi:10.1073/pnas.97.10.5440

720 23. Chikahisa S, Shimizu N, Shiuchi T, Séi H. Ketone body metabolism and sleep
721 homeostasis in mice. Neuropharmacology. 2014;79:399-404.
722 doi:10.1016/j.neuropharm.2013.12.009

723 24. Puchalska P, Crawford PA. Multi-dimensional Roles of Ketone Bodies in Fuel Metabolism,
724 Signaling, and Therapeutics. Cell Metab. 2017;25(2):262-284. doi:10.1016/j.cmet.2016.12.022

725 25. Ma W, Berg J, Yellen G. Ketogenic diet metabolites reduce firing in central neurons by
726 opening K(ATP) channels. J Neurosci. 2007;27(14):3618-3625. doi:10.1523/JNEUROSCI.0132-
727 07.2007

728 26. Jensen NJ, Wodschow HZ, Nilsson M, Rungby J. Effects of Ketone Bodies on Brain
729 Metabolism and Function in Neurodegenerative Diseases. Int J Mol Sci. 2020;21(22):8767.
730 Published 2020 Nov 20. doi:10.3390/ijms21228767

731 27. Hartman AL, Gasior M, Vining EP, Rogawski MA. The neuropharmacology of the
732 ketogenic diet. Pediatr Neurol. 2007;36(5):281-292. doi:10.1016/j.pediatrneurol.2007.02.008

733 28. Xin L, Ipek Ö, Beaumont M, et al. Nutritional Ketosis Increases NAD+/NADH Ratio in
734 Healthy Human Brain: An in Vivo Study by 31P-MRS. Front Nutr. 2018;5:62. Published 2018 Jul
735 12. doi:10.3389/fnut.2018.00062

736 29. Maalouf M, Sullivan PG, Davis L, Kim DY, Rho JM. Ketones inhibit mitochondrial
737 production of reactive oxygen species production following glutamate excitotoxicity by increasing
738 NADH oxidation. Neuroscience. 2007;145(1):256-264. doi:10.1016/j.neuroscience.2006.11.06

739 30. Shimazu T, Hirschey MD, Newman J, et al. Suppression of oxidative stress by β-
740 hydroxybutyrate, an endogenous histone deacetylase inhibitor. Science. 2013;339(6116):211-
741 214. doi:10.1126/science.1227166

742 31. Lutas A, Yellen G. The ketogenic diet: metabolic influences on brain excitability and
743 epilepsy. Trends Neurosci. 2013;36(1):32-40. doi:10.1016/j.tins.2012.11.005

744 32. Clarke K, Tchabanenko K, Pawlosky R, et al. Kinetics, safety and tolerability of (R)-3-
745 hydroxybutyl (R)-3-hydroxybutyrate in healthy adult subjects. Regul Toxicol Pharmacol.
746 2012;63(3):401-408. doi:10.1016/j.yrtph.2012.04.008

747 33. Kesl SL, Poff AM, Ward NP, et al. Effects of exogenous ketone supplementation on blood
748 ketone, glucose, triglyceride, and lipoprotein levels in Sprague-Dawley rats. Nutr Metab (Lond).
749 2016;13:9. Published 2016 Feb 4. doi:10.1186/s12986-016-0069-y

750 34. Weistuch C, Mujica-Parodi LR, Razban RM, et al. Metabolism modulates network
751 synchrony in the aging brain. Proc Natl Acad Sci U S A. 2021;118(40):e2025727118.
752 doi:10.1073/pnas.2025727118

753 35. Mujica-Parodi LR, Amgalan A, Sultan SF, et al. Diet modulates brain network stability, a
754 biomarker for brain aging, in young adults. Proc Natl Acad Sci U S A. 2020;117(11):6170-6177.
755 doi:10.1073/pnas.1913042117

756 36. Hruz PW, Murata H, Qiu H, Mueckler M. Indinavir induces acute and reversible peripheral
757 insulin resistance in rats. Diabetes. 2002;51(4):937-942. doi:10.2337/diabetes.51.4.937

758 37. Hresko RC, Hruz PW. HIV protease inhibitors act as competitive inhibitors of the
759 cytoplasmic glucose binding site of GLUTs with differing affinities for GLUT1 and GLUT4. PLoS
760 One. 2011;6(9):e25237. doi:10.1371/journal.pone.0025237

761 38. de Lores Arnaiz GR, Ordieres MG. Brain Na(+), K(+)-ATPase Activity In Aging and Disease.
762 Int J Biomed Sci. 2014;10(2):85-102.

763 39. Colgin LL, Denninger T, Fyhn M, et al. Frequency of gamma oscillations routes flow of
764 information in the hippocampus. Nature. 2009;462(7271):353-357. doi:10.1038/nature0857340.
765 Buzsáki G, Wang XJ. Mechanisms of gamma oscillations. Annu Rev Neurosci.
766 2012;35:203-225. doi:10.1146/annurev-neuro-062111-1444

767 41. Catterall WA. From ionic currents to molecular mechanisms: the structure and function of
768 voltage-gated sodium channels. Neuron. 2000;26(1):13-25. doi:10.1016/s0896-6273(00)81133-2

769 42. Howarth C, Gleeson P, Attwell D. Updated energy budgets for neural computation in the
770 neocortex and cerebellum. J Cereb Blood Flow Metab. 2012;32(7):1222-1232.
771 doi:10.1038/jcbfm.2012.35

772 43. Lujan B, Kushmerick C, Banerjee TD, Dagda RK, Renden R. Glycolysis selectively shapes
773 the presynaptic action potential waveform. J Neurophysiol. 2016;116(6):2523-2540.
774 doi:10.1152/jn.00629.2016

775 44. Padamsey Z, Katsanevaki D, Dupuy N, Rochefort NL. Neocortex saves energy by
776 reducing coding precision during food scarcity. Neuron. 2022;110(2):280-296.e10.
777 doi:10.1016/j.neuron.2021.10.024

778 45. Jensen TP, Zheng K, Cole N, Marvin JS, Looger LL, Rusakov DA. Multiplex imaging
779 relates quantal glutamate release to presynaptic Ca2+ homeostasis at multiple synapses in situ.
780 Nat Commun. 2019;10(1):1414. Published 2019 Mar 29. doi:10.1038/s41467-019-09216-8

781 46. Newman JC, Verdin E. β-Hydroxybutyrate: A Signaling Metabolite. Annu Rev Nutr.
782 2017;37:51-76. doi:10.1146/annurev-nutr-071816-064916

783 47. Lund TM, Obel LF, Risa Ø, Sonnewald U. β-Hydroxybutyrate is the preferred substrate for
784 GABA and glutamate synthesis while glucose is indispensable during depolarization in cultured
785 GABAergic neurons. Neurochem Int. 2011;59(2):309-318. doi:10.1016/j.neuint.2011.06.002

786 48. Scott RS, Henneberger C, Padmashri R, Anders S, Jensen TP, Rusakov DA. Neuronal
787 adaptation involves rapid expansion of the action potential initiation site. *Nat Commun*.
788 2014;5:3817. Published 2014 May 23. doi:10.1038/ncomms4817

789 49. Stranahan AM, Mattson MP. Impact of energy intake and expenditure on neuronal
790 plasticity. Neuromolecular Med. 2008;10(4):209-218. doi:10.1007/s12017-008-8043-0

791 50. Piroli GG, Grillo CA, Reznikov LR, et al. Corticosterone impairs insulin-stimulated
792 translocation of GLUT4 in the rat hippocampus. Neuroendocrinology. 2007;85(2):71-80.
793 doi:10.1159/000101694

794 51. Grillo CA, Piroli GG, Hendry RM, Reagan LP. Insulin-stimulated translocation of GLUT4
795 to the plasma membrane in rat hippocampus is PI3-kinase dependent. Brain Res. 2009;1296:35-
796 45. doi:10.1016/j.brainres.2009.08.005

797 52. Leloup C, Arluison M, Kassis N, et al. Discrete brain areas express the insulin-responsive
798 glucose transporter GLUT4. Brain Res Mol Brain Res. 1996;38(1):45-53. doi:10.1016/0169-
799 328x(95)00306-d

800 53. Vannucci SJ, Koehler-Stec EM, Li K, Reynolds TH, Clark R, Simpson IA. GLUT4 glucose
801 transporter expression in rodent brain: effect of diabetes. Brain Res. 1998;797(1):1-11.
802 doi:10.1016/s0006-8993(98)00103-6

803 54. Miranda M, Morici JF, Zanoni MB, Bekinschtein P. Brain-Derived Neurotrophic Factor: A
804 Key Molecule for Memory in the Healthy and the Pathological Brain. Front Cell Neurosci.
805 2019;13:363. Published 2019 Aug 7. doi:10.3389/fncel.2019.00363

806 55. Won SJ, Yoo BH, Kauppinen TM, et al. Recurrent/moderate hypoglycemia induces
807 hippocampal dendritic injury, microglial activation, and cognitive impairment in diabetic rats. J
808 Neuroinflammation. 2012;9:182. Published 2012 Jul 25. doi:10.1186/1742-2094-9-182

809 56. Yamada KA, Rensing N, Izumi Y, et al. Repetitive hypoglycemia in young rats impairs
810 hippocampal long-term potentiation. Pediatr Res. 2004;55(3):372-379.
811 doi:10.1203/01.PDR.0000110523.07240.C

812 57. Lee SY, Kim JH. Mechanisms underlying presynaptic Ca2+ transient and vesicular
813 glutamate release at a CNS nerve terminal during in vitro ischaemia. J Physiol.
814 2015;593(13):2793-2806. doi:10.1113/JP270060

815 58. García-Rodríguez D, Giménez-Cassina A. Ketone Bodies in the Brain Beyond Fuel

816 Metabolism: From Excitability to Gene Expression and Cell Signaling. Front Mol Neurosci.
817 2021;14:732120. Published 2021 Aug 27. doi:10.3389/fnmol.2021.732120
818
819 59. van Nieuwenhuizen, H., Chesebro, A. G., Polizu, C., Clarke, K., Strey, H. H., Weistuch,
820 C., & Mujica-Parodi, L. R. Ketosis regulates K+ ion channels, strengthening brain-wide signaling
821 disrupted by age. *bioRxiv*, 2023-05.

822 60. Ma W, Berg J, Yellen G. Ketogenic diet metabolites reduce firing in central neurons by
823 opening K(ATP) channels. J Neurosci. 2007;27(14):3618-3625. doi:10.1523/JNEUROSCI.0132-
824 07.2007

825 61. Tanner GR, Lutas A, Martínez-François JR, Yellen G. Single K ATP channel opening in
826 response to action potential firing in mouse dentate granule neurons. J Neurosci.
827 2011;31(23):8689-8696. doi:10.1523/JNEUROSCI.5951-10.2011

828 62. Martínez-François JR, Fernández-Agüera MC, Nathwani N, et al. BAD and KATP
829 channels regulate neuron excitability and epileptiform activity. Elife. 2018;7:e32721. Published
830 2018 Jan 25. doi:10.7554/eLife.32721

831 63. Lund TM, Ploug KB, Iversen A, Jensen AA, Jansen-Olesen I. The metabolic impact of β-
832 hydroxybutyrate on neurotransmission: Reduced glycolysis mediates changes in calcium
833 responses and KATP channel receptor sensitivity. J Neurochem. 2015;132(5):520-531.
834 doi:10.1111/jnc.12975

835 64. He H, Mahnke AH, Doyle S, et al. Neurodevelopmental role for VGLUT2 in pyramidal
836 neuron plasticity, dendritic refinement, and in spatial learning. *J Neurosci*. 2012;32(45):15886-
837 15901. doi:10.1523/JNEUROSCI.4505-11.2012

838 65. Juge N, Gray JA, Omote H, et al. Metabolic control of vesicular glutamate transport and
839 release. Neuron. 2010;68(1):99-112. doi:10.1016/j.neuron.2010.09.002

840 66. Centers for Disease Control and Prevention. National Diabetes Statistics Report website.
841 https://www.cdc.gov/diabetes/data/statistics-report/index.html Last Reviewed November 29,
842 2023. Accessed April 18, 2024.67. Pernía-Andrade AJ, Goswami SP, Stickler Y, Fröbe U,
843 Schlögl A, Jonas P. A deconvolution-based method with high sensitivity and temporal resolution
844 for detection of spontaneous synaptic currents in vitro and in vivo. Biophys J. 2012;103(7):1429-
845 1439. doi:10.1016/j.bpj.2012.08.039

846 68. Koch C, Chapter 6: The Hodgkin and Huxley Model of Action Potential Generation. In:
847 Koch C, Biophysics of Computation: Information Processing in Single Neurons. Oxford University
848 Press. 2004. p. 139-176. Print.

849 69. Traub RD, Wong RK, Miles R, Michelson H. A model of a CA3 hippocampal pyramidal
850 neuron incorporating voltage-clamp data on intrinsic conductances. J Neurophysiol.

1991;66(2):635-6. doi:10.1152/jn.1991.66.2.635

70. Yu N, Morris CE, Joós B, Longtin A. Spontaneous excitation patterns computed for axons with injury-like impairments of sodium channels and Na/K pumps. PLoS Comput Biol. 2012;8(9):e1002664. doi:10.1371/journal.pcbi.1002664

71. Altemus KL, Lavenex P, Ishizuka N, Amaral DG. Morphological characteristics and electrophysiological properties of CA1 pyramidal neurons in macaque monkeys. Neuroscience. 2005;136(3):741-756. doi:10.1016/j.neuroscience.2005.07.001

13. **Figures Legends.**

Figure 1: Synaptic activity and LTP, but not neuronal firing or PPR, decrease during paired stimulation under AIR conditions and do not recover during D-βHb administration.

A) Scatter plot of the fEPSP amplitudes evoked by paired-pulse stimulation of Schaffer collaterals. Each pair of circles is the average of 30-40 consecutive responses. The black bars represent the mean ± SEM. Control fEPSPs in gray, AIR in red; 0.1 mM D-βHb+AIR in blue; 1 mM D-βHb+AIR in purple. Control: n=26 slices; AIR n=19; 0.1 mM D-βHb+AIR: n=20; 1 mM D-βHb+AIR: n=16. B) Scatter plot of the paired-pulse ratio (PPR) of the fEPSPs recorded in A. The labels, n, are identical to those in A). There were no significant differences (p=0.41, ANOVA). C) On top: Representative recording of a control experiment in which paired stimulation was applied for 50 min. Each circle represents the fEPSP amplitude normalized to the average of the first 30 fEPSPs. The dashed orange line represents the mean amplitude at time -10 to 0 min. The black line represents the mean amplitude at +30 to +40 min. Bottom: corresponding normalized PPR. D) fEPSP waveforms recorded in C), showing LTP development. In gray, 30 fEPSP waveforms at t=0 ± 5 min and their average (black). In yellow, 30 fEPSP waveforms at t=+30 ± 5 min and their average (orange). Stimulation artifacts and FVs are removed. E) Scatter plot of LTP signals triggered by paired stimulation. Control: n=13; AIR n=11; 0.1 mM D-βHb+AIR: n=12; 1 mM D-βHb+AIR: n=14. F) Scatter plot of the FV amplitudes recorded during A). The labels, n, are identical to those in A). There were no significant differences (p=0.42, p=0.40; ANOVA). In all plots, *p<0.05; **p<0.01; ***p<0.001.

Figure 2: Conduction velocity (CV) of Schaffer collaterals decreases under AIR conditions, is rescued by 0.1 mM D-βHb, and increases with 1 mM D-βHb.

A) Representative hippocampal slice during CV recording. B) Representative averaged FV waveforms recorded in CA1. The stimulus onset time (t=0) is marked with a dashed line. Stimulus artifacts are removed. C) CV scatter plots. Each colored circle represents a CV replicate. Control in gray, AIR in light red, 0.1 mM D-βHb+AIR in blue, and 1 mM D-βHb+AIR in purple. Data are shown as the mean ± SEM. *p<0.05; ***p<0.001, nested ANOVA, Control: m=62, n=24, N=14; AIR: m=65, n=22, N=13; 0.1 mM D-βHb+AIR: m=64, n=21, N=13; 1 mM D-βHb+AIR: m=50, n=14,

N=10. D) Diagram of the CV of an AP propagating along an axon: distance along the axon (Δx) and the time needed for an AP to pass that distance (t_2-t_1). V represents the membrane potential. E) Model of a propagating AP. The change in V(t) is shown at longitudinal increments along the axon (x_2) and at neighboring increments immediately before (x_1) and behind (x_3). The membrane potential at rest (V_R) changes over time proportionally to the sum of differences between its value and those of the preceding and superseding increments. Upon reaching the threshold potential (V_T), a spike occurs, and the membrane potential reaches the peak value (VA). F-G) CV is modulated by V_A and V_R. Our computational model predicts declining CV due to reductions in the peak AP (F) and/or hyperpolarization of the resting membrane potential (G). The CV is quantified as a percentage relative to the control.

Figure 3: Time delays in axonal firing during train stimulation are increased during AIR and reversed by 1 mM D-βHb.

A) Top: Representative example of the FVs recorded at the first stimulus in the control group during stimulation with 20 pulses applied at 25 Hz every 20 s over 20 min. Bottom: FVs recorded in response to the last stimulus in each train. The FVs recorded at t=0 are marked in black; the FVs recorded at t=+20 min are marked in dark gray. B) - D) The same as A) in the AIR, 0.1 mM D-βHb+AIR and 1 mM D-βHb+AIR groups. E) Heatmap of the mean, normalized FV peak latencies recorded in the Control group. Each trial is represented by a new row. The columns represent the time points of successive stimuli. Normalized latencies (0 ms) are color-coded in yellow. Delays (>0 ms) are color-coded in green–violet, and latency improvements (<0 ms) are color-coded in orange–brown. n=24, N=22. F) - H) The same as E) for AIR, n=16, N=15; 0.1 mM D-βHb+AIR. n=17, N=15, 1 mM D-βHb+AIR. n=14, N=10. I) Statistical comparison of latencies for the Control (E) and AIR (F) groups, performed based on means of 3 stimuli x 2 trials blocks. $p<0.05$ in green, $p<0.1$ in yellow, $p\geq0.1$ in white. J) The same as I) comparing the results of the Control (E) and 1 mM D-βHb+AIR (H) groups. There were no significant differences, p=0.067 to p=0.99. K) The same as I) comparing the results of the AIR (F) and 0.1 mM D-βHb+AIR (G) groups. There were no significant differences, p=0.41 to p=0.99. L) The same as I) comparing the results of the AIR (F) and 1 mM D-βHb+AIR (H) groups.

Figure 4: Membrane resistance (R_m) increases during AIR and is not reversed by D-βHb. Other intrinsic properties did not change under either condition.

A) Left: A CA1 pyramidal neuron recorded in whole-cell patch-clamp mode (outlined in red), with resistances and capacitance denoted within the cell. Right: A simple electric circuit diagram of a cell with the same resistances. B) Scatter plots of CA1 pyramidal neuron Rm compared among the experimental groups. Each colored circle represents a value recorded in a single cell. Control in gray, AIR in light red, 1 mM D-βHb+AIR in purple. Vertical black bars represent the mean ± SEM. C) Scatter plots of CA1 pyramidal neurons C_m compared among the experimental groups. The plots and coloring are identical to B). There were no significant differences (p=0.32). D)

927 Representative example of a 300 pA ramp current injection performed in a control CA1 pyramidal
928 neuron. The dashed line marks the onset (spike threshold) of the first AP. The inset shows the
929 magnified appreciate, with the arrow pointing to the onset. E) Scatter plots of CA1 pyramidal
930 neuron spike thresholds compared among the experimental groups. The plots are identical to B).
931 There were no significant differences (p=0.17). F) Scatter plots of CA1 pyramidal neurons RMP
932 (V_{rest}) compared among the experimental groups. The plots and coloring are identical to B). There
933 were no significant differences (p=0.09). Control n=28, N=22; AIR n=25, N=17; 1 mM D-βHb+AIR;
934 n=30, N=16. In black, *p<0.05; **p<0.01; ***p<0.001; in gray *p<0.1.3.3 AIR adversely affects
935 input timing, which is restored by high D-βHb concentrations.

936

937 **Figure 5**: AIR increased sEPSC frequency without altering sEPSC properties, and D-βHb
938 administration did not reverse this effect.

939 A) Representative examples of the first 2 min of sEPSC waveforms recorded in CA1 pyramidal
940 neurons, voltage clamped at V_h= -70 mV (Control in gray; AIR in red; 1.0 mM D-βHb+AIR in
941 purple). Bottom: averaged sEPSC waveforms from individual cells (light color) and the group
942 mean (full color). B) Scatter plots of the sEPSC frequency recorded in CA1 pyramidal neurons
943 compared among the experimental groups. Each colored circle represents the frequency
944 recorded in a single cell. The labels are the same as in A). Vertical black bars represent the mean
945 ± SEM. *p<0.05. C) Scatter plots of the sEPSC 20-80% rise times, labeled as in B). There were
946 no significant differences (p=0.51). D) Scatter plots of the sEPSC decay tau times, labeled as in
947 B). There were no significant differences (p=0.98). E) Scatter plots of the sEPSC amplitudes,
948 labeled as in B). There were no significant differences (p=0.21). Control n=19, N=19; AIR n=19,
949 N=14; 1 mM D-βHb+AIR, n=23, N=16. **p<0.01.

950

951 **Figure 6**: Neuronal firing is mildly affected by AIR and reversed by D-βHb, with D-βHb increasing
952 AP overshoot amplitudes.

953 A) Representative examples of responses to 400 pA square current injections into control (gray),
954 AIR (red), and 1 mM D-βHb+AIR (purple) CA1 pyramidal neurons, held at V_h=-70 mV. B) I-O
955 curves of CA1 pyramidal neurons receiving 21, Δ+25 pA injections (max. 0 pA; V_h=-70 mV).
956 Circles represent the group mean ± SEM. * Control vs. AIR, + Control vs. 1 mM D-βHb+AIR, ^
957 AIR vs. 1 mM D-βHb+AIR. *,+,^ in black p<0.05; **,++,^^ in black p<0.01; *,+,^ in gray p<0.1;
958 ANOVA) Maximum firing rate of the pyramidal neurons in B). Circles represent single neurons;
959 black bars represent group mean ± SEM. There were no significant differences (p=0.778,
960 ANOVA). D) Example of responses to Δ+25 pA square current injections into a control pyramidal
961 neuron. The arrowhead and inset mark the final membrane depolarization (V_m, last 5 ms of the
962 step). E) Vm at the current injections from B). F) Group mean ± SEM of V_m from E). Statistical
963 tests and labels are identical to B). Control n=23, N=20; AIR n=20, N=14; 1 mM D-βHb+AIR n=22,
964 N=16. G) Example of AP overshoot measurement. The black line marks V_m= 0 mV. H) Averaged
965 AP overshoot amplitudes from B). I) Group mean ± SEM of overshoot amplitudes from H).

Statistical tests and labels are identical to B). In all comparisons, Control n=23, N=20; AIR n=20, N=14; 1 mM D-βHb+AIR, n=22, N=16.

Figure 7: AP decay times change during AIR and D-βHb + AIR conditions, but D-βHb + AIR APs have faster rise times.

A) Example of AP decay time measurement. The black line marks V_m= 0 mV. B) Mean AP decay times for the current injections. Circles represent averaged amplitudes in single neurons. The black lines represent group means. C) Group mean ± SEM of AP decay times from B). Statistical tests and labels are identical to B). D) Example of AP decay time measurement. The black line marks V_m= 0 mV. E) Averaged AP rise times for the current injections in B). Circles represent averaged amplitudes in single neurons. The black lines represent group means. F) Group mean ± SEM of AP rise times from B). Statistical tests and labels are identical to B). G) An example of the AP IEI measurement. The double arrow marks the latency between AP peaks. H) Averaged IEI recorded during the injections in B). Each point represents the average IEI recorded at each step in a single neuron. The black line represents the group mean. I) Group mean ± SEM of averaged IEI. *,+,^ $p<0.05$; ANOVA. In all comparisons, Control n=23, N=20; AIR n=20, N=14; 1 mM D-βHb+AIR, n=22, N=16.

Figure 1.

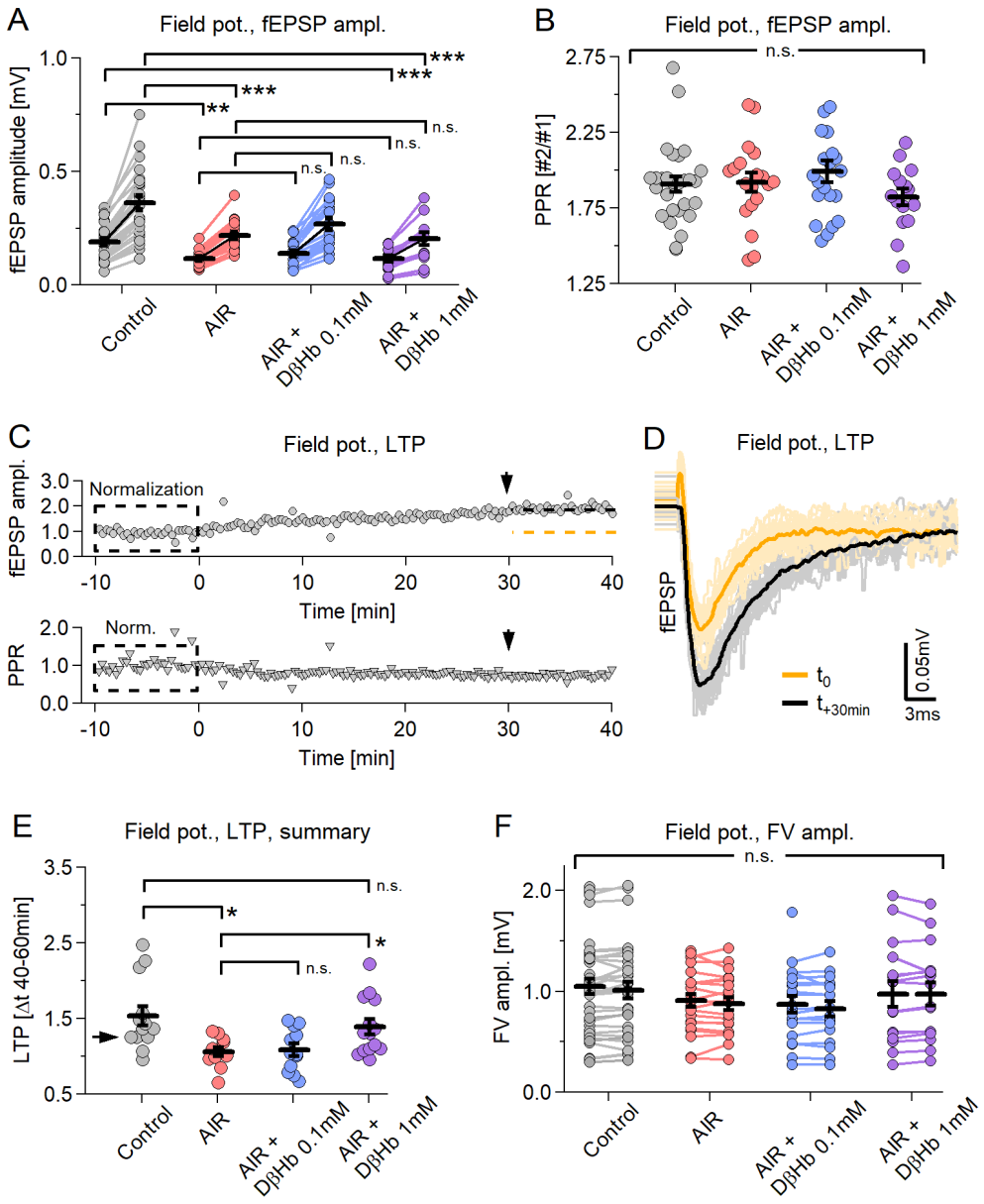
A
Field pot., fEPSP ampl.
fEPSP amplitude [mV]
1.0
0.5
0.0
***
***
**
***
n.s.
n.s.
n.s.
Control
AIR
AIR + DβHb 0.1mM
AIR + DβHb 1mM
B
Field pot., fEPSP ampl.
PPR [#2/#1]
2.75
2.25
1.75
1.25
n.s.
Control
AIR
AIR + DβHb 0.1mM
AIR + DβHb 1mM
C
Field pot., LTP
fEPSP ampl.
3.0
2.0
1.0
0.0
Normalization
-10
0
10
20
30
40
Time [min]
PPR
2.0
1.0
0.0
Norm.
-10
0
10
20
30
40
Time [min]
D
Field pot., LTP
fEPSP
t_0
t_{+30min}
0.05mV
3ms
E
Field pot., LTP, summary
LTP [Δt 40-60min]
3.5
2.5
1.5
0.5
n.s.
*
*
n.s.
Control
AIR
AIR + DβHb 0.1mM
AIR + DβHb 1mM
F
Field pot., FV ampl.
FV ampl. [mV]
2.0
1.0
0.0
n.s.
Control
AIR
AIR + DβHb 0.1mM
AIR + DβHb 1mM

Figure 2.

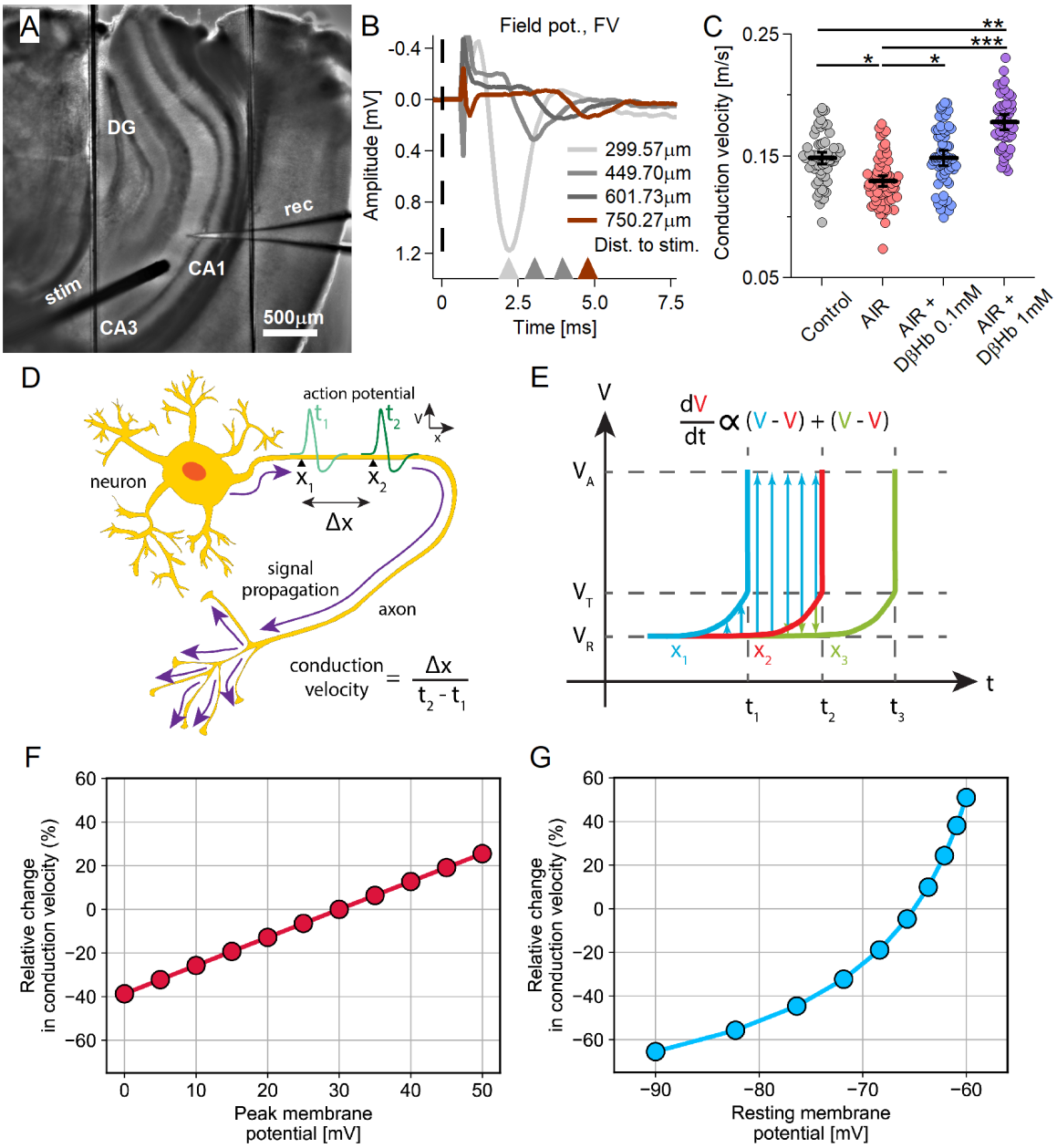
A
DG
rec
CA1
stim
CA3
500µm
B
Field pot., FV
Amplitude [mV]
-0.4
0.0
0.4
0.8
1.2
299.57µm
449.70µm
601.73µm
750.27µm
Dist. to stim.
0
2.5
5.0
7.5
Time [ms]
C
Conduction velocity [m/s]
0.25
0.15
0.05
*
*
**
***
Control
AIR
AIR + DβHb 0.1mM
AIR + DβHb 1mM
D
action potential
neuron
signal propagation
axon
Δx
conduction velocity = Δx / (t2 - t1)
E
V
dV/dt ∝ (V - V) + (V - V)
VA
VT
VR
t
F
Relative change in conduction velocity (%)
Peak membrane potential [mV]
G
Relative change in conduction velocity (%)
Resting membrane potential [mV]

Figure 3.

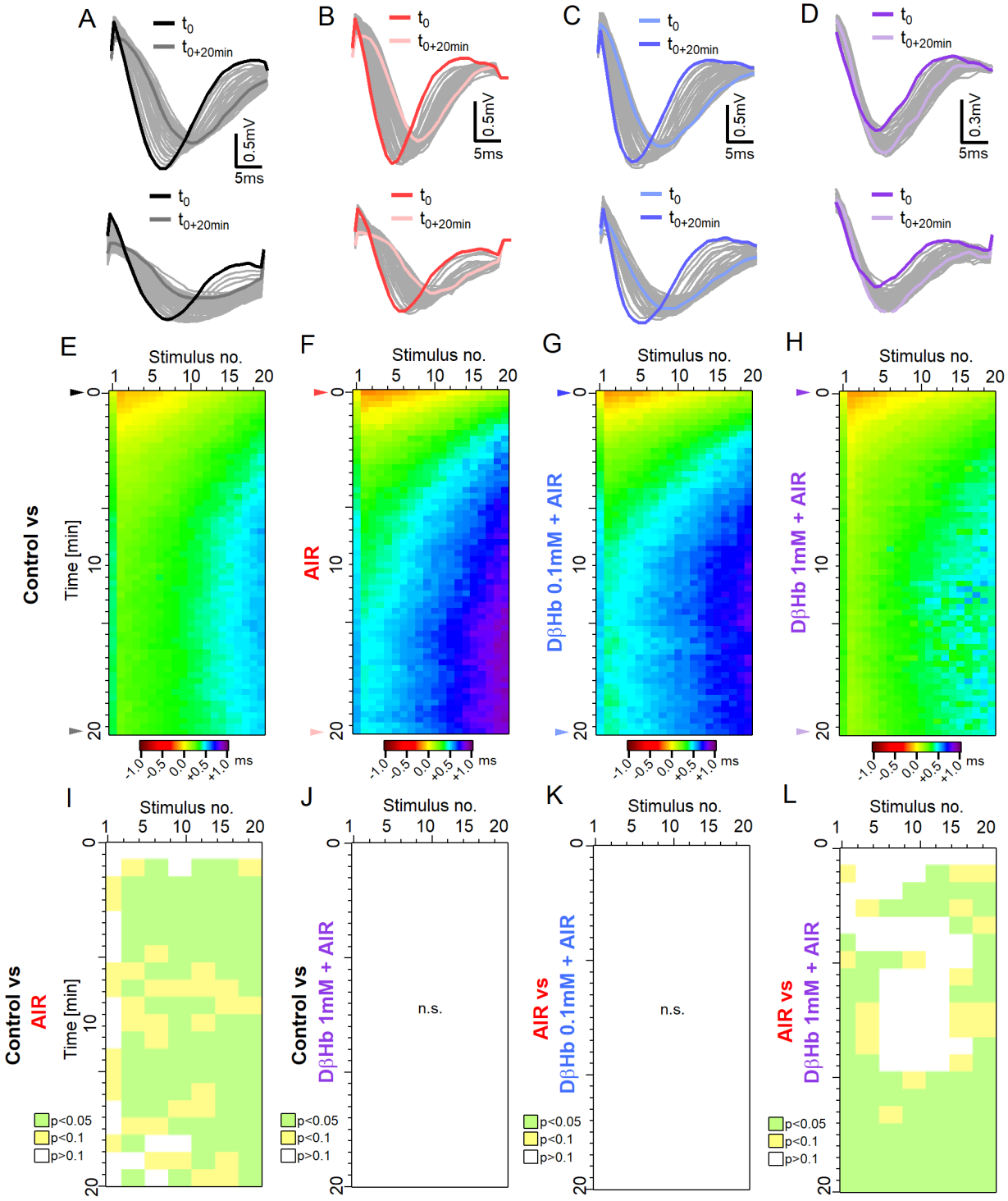
A
B
C
D
t_0
$t_{0+20min}$
0.5mV
0.3mV
5ms
E
F
G
H
Stimulus no.
Time [min]
Control vs
AIR
DβHb 0.1mM + AIR
DβHb 1mM + AIR
-1.0 -0.5 0.0 +0.5 +1.0 ms
I
J
K
L
AIR vs
n.s.
p<0.05
p<0.1
p>0.1

Figure 4.

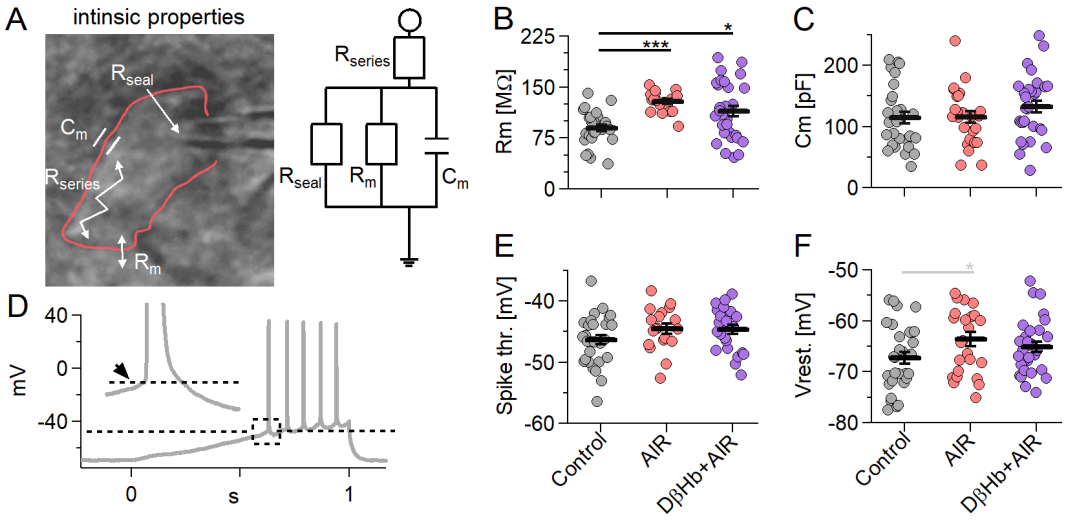
A
intinsic properties
Rseal
Cm
Rseries
Rm
Rseries
Rseal
Rm
Cm
B
225
150
75
0
Rm [MΩ]
***
*
C
200
100
0
Cm [pF]
D
40
0
-40
mV
0
s
1
E
-40
-50
-60
Spike thr. [mV]
F
-50
-60
-70
-80
Vrest. [mV]
*
Control
AIR
DβHb+AIR
Control
AIR
DβHb+AIR

Figure 5.

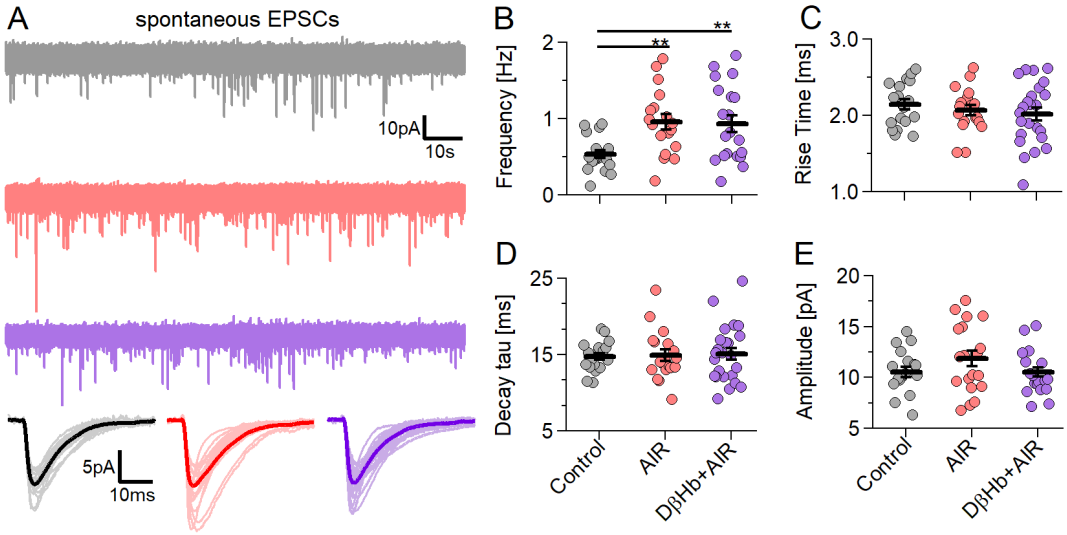
A
spontaneous EPSCs
10pA
10s
5pA
10ms
B
Frequency [Hz]
2
1
0
**
**
C
Rise Time [ms]
3.0
2.0
1.0
D
Decay tau [ms]
25
15
5
E
Amplitude [pA]
20
15
10
5
Control
AIR
DβHb+AIR

Figure 6.

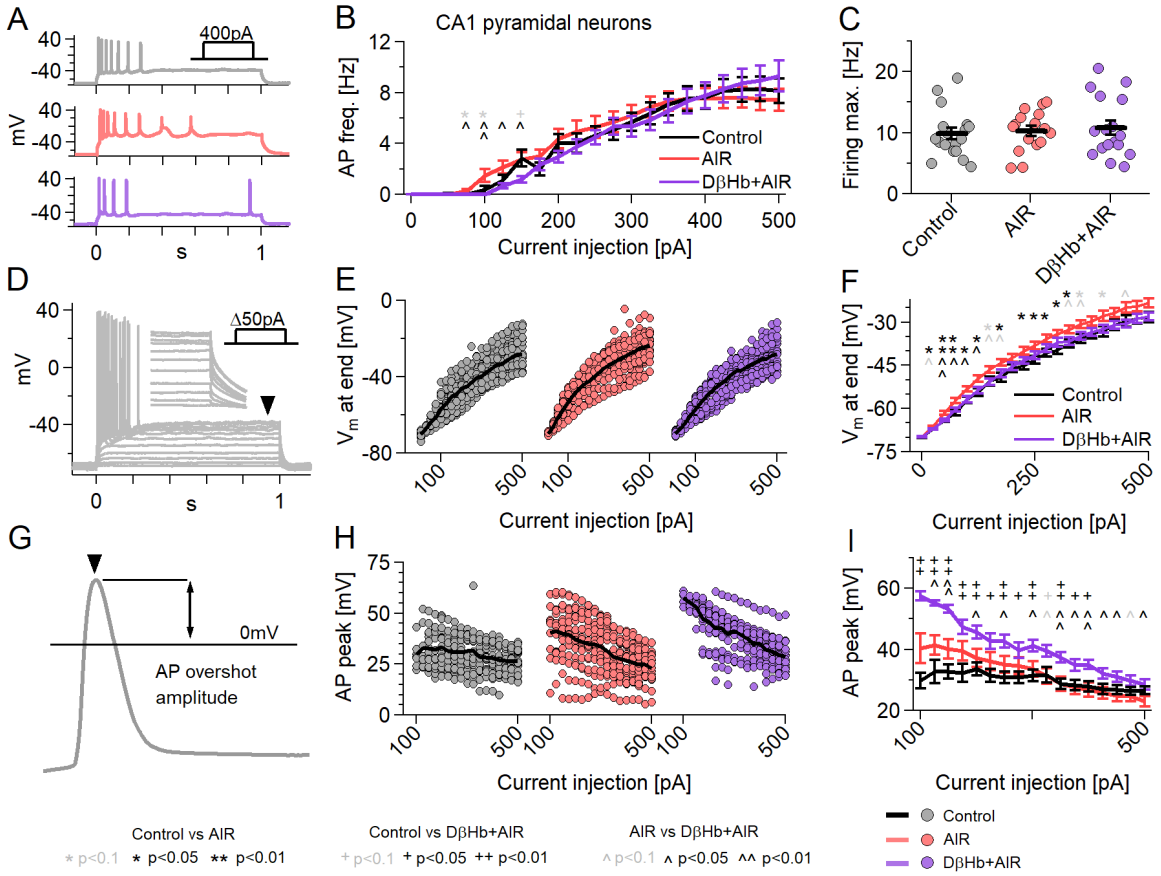
A
400pA
mV
s
B
CA1 pyramidal neurons
AP freq. [Hz]
Current injection [pA]
Control
AIR
DβHb+AIR
C
Firing max. [Hz]
Control
AIR
DβHb+AIR
D
Δ50pA
mV
s
E
Vm at end [mV]
Current injection [pA]
F
Vm at end [mV]
Current injection [pA]
Control
AIR
DβHb+AIR
G
0mV
AP overshot
amplitude
H
AP peak [mV]
Current injection [pA]
I
AP peak [mV]
Current injection [pA]
Control
AIR
DβHb+AIR
Control vs AIR
* p<0.1 * p<0.05 ** p<0.01
Control vs DβHb+AIR
+ p<0.1 + p<0.05 ++ p<0.01
AIR vs DβHb+AIR
^ p<0.1 ^ p<0.05 ^^ p<0.01

Figure 7.

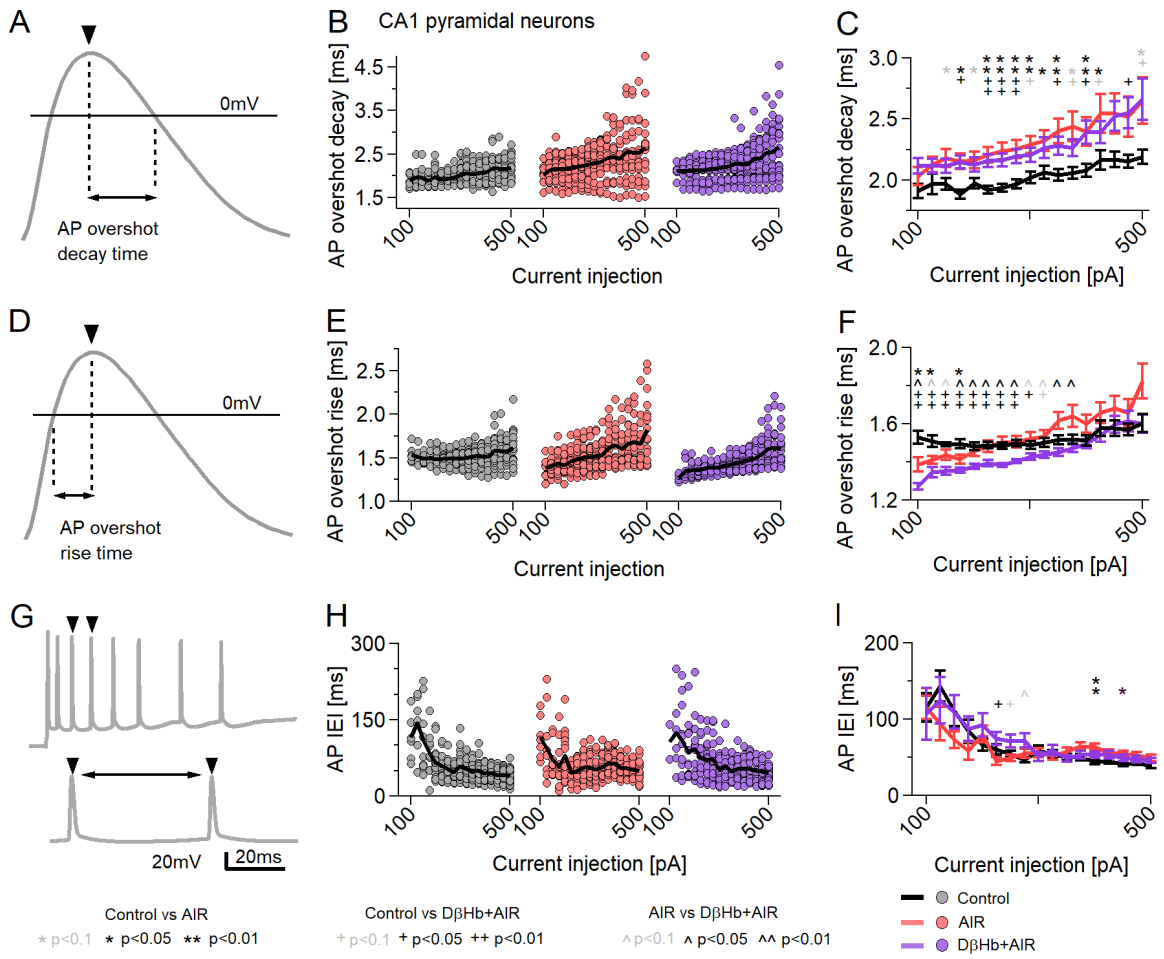
A
0mV
AP overshot
decay time
B
CA1 pyramidal neurons
AP overshot decay [ms]
Current injection
C
AP overshot decay [ms]
Current injection [pA]
D
0mV
AP overshot
rise time
E
AP overshot rise [ms]
Current injection
F
AP overshot rise [ms]
Current injection [pA]
G
20mV
20ms
H
AP IEI [ms]
Current injection [pA]
I
AP IEI [ms]
Current injection [pA]
Control
AIR
DβHb+AIR
Control vs AIR
* p<0.1 * p<0.05 ** p<0.01
Control vs DβHb+AIR
+ p<0.1 + p<0.05 ++ p<0.01
AIR vs DβHb+AIR
^ p<0.1 ^ p<0.05 ^^ p<0.01